International Journal of Engineering Science 225 (2026) 104554

Contents lists available at ScienceDirect

International Journal of Engineering Science

journal homepage: www.elsevier.com/locate/ijengsci

Full length article

Phase-field modeling and simulations for dendrite growth in electrodeposition

Maria Chiara D'Autilia [a], Ivonne Sgura [a,*], Massimo Frittelli [a], Benedetto Bozzini [b]

[a] University of Salento, Department of Mathematics and Physics "E.De Giorgi", Lecce, 73100, Italy
[b] Politecnico di Milano, Department of Energy, Milano, 20156, Italy

ARTICLE INFO

Keywords:
Dendrites
Rechargeable metal batteries
Electrodeposition
Metal plating
Phase-field modeling
Matrix-oriented finite differences

ABSTRACT

This work presents a phase-field differential model for simulating dendritic growth during metal electrodeposition, of special relevance to the operation of rechargeable batteries with metal anodes, such as: lithium, sodium and zinc. The model modifies the well-assessed phase-field model for dendritic crystal growth by Kobayashi, replacing the thermal field by a concentration field for the electroactive species in the electrolyte, that couples electrochemically to the local potential difference across the electrode-electrolyte interface. Such concentration is governed by a mass transport equation that accounts for electrochemical effects. The resulting nonlinear system of PDEs is spatially discretized using finite differences and integrated explicitly in time. Numerical simulations illustrate how the kinetic coefficient, anisotropy mode number, and dimensionless current density influence the evolution and morphology of dendritic structures. We introduce morphological indicators to quantitatively analyze the simulated dendrites: fractal dimension, skeleton-based metrics, and the inverse isoperimetric quotient (IIQ). Based on the IIQ analysis, we provide a segmentation of the parameter space to reproduce key features of electrochemical dendrite formation. We present comparisons with micrographs of experimental dendrites to validate our results.

1. Introduction

Metal electrodeposition or electroplating is a widespread technology which finds application in diverse fields, such as: primary metallurgy, metal shaping, fabrication of contacts in semiconductor, surface finishing and rechargeable batteries. Notwithstanding a time-honored history and an immense literature background, shape control during metal growth is a complex problem, impacting the quality of the material or the durability of the device aspect. A definitive and general understanding of the factors affecting the formation of unstable shapes, dendrites in particular, is still lacking a definitive understanding. This condition is particularly critical for battery science and technology, since use of metal anodes is one of the key approaches in view of increasing battery energy- and power-density and developing sustainable battery chemistries, but lack of plating control is currently preventing practical implementation of these devices. The topic is particularly hot for zinc-based batteries, that are the safest, cheapest and most sustainable option among chemistries featuring a metallic anode. Recent experimental and modeling studies have focused on understanding and mitigating dendrite formation, highlighting the need for accurate predictive tools (He et al., 2024; Jian et al., 2024; Yuan et al., 2024). For instance, He et al. (2024) combined experimental observations with multiphysics modeling to study

* Corresponding author.
E-mail address: ivonne.sgura@unisalento.it (I. Sgura).

https://doi.org/10.1016/j.ijengsci.2026.104554
Received 24 February 2026; Received in revised form 3 April 2026; Accepted 16 April 2026
Available online 25 April 2026

dendrite growth and suppression mechanisms in zinc-air batteries, while Jian et al. (2024) developed phase-field simulations coupled with heat and mass transfer to analyze zinc dendrites under various electrolyte conditions. Yuan et al. (2024) investigated alloying strategies to inhibit dendrite growth, supported by modeling insights into morphological evolution.

The state-of-the-art modeling of electrodeposition increasingly relies on phase-field methods, which offer a powerful and versatile framework to capture the complex morphological evolution of electrodeposited structures by representing interfaces implicitly through continuous order parameters (Arguello et al., 2022a, 2022b, 2023; Chen et al., 2015; Hong & Viswanathan, 2018; Kobayashi, 1993; Liang et al., 2012). These models incorporate electrochemical kinetics, ion transport, and interfacial energy anisotropy to simulate dendritic growth under realistic electrochemical operating conditions. The high fidelity and predictive capability of phase-field simulations make them invaluable tools for designing dendrite suppression strategies and optimizing plating uniformity. Numerous studies have developed advanced phase-field models featuring coupled nonlinear partial differential equations that describe the interplay between electric potential, concentration fields, and phase evolution The computational cost of these simulations is often high due to the need for fine spatial and temporal resolution to resolve dendrite tips and capture the highly nonlinear dynamics. This stream of literature on phase-field modeling was kick-started by Kobayashi's seminal work (Kobayashi, 1993), where dendritic crystal growth was first modeled through a phase-field system that focuses on the effects of anisotropy and undercooling. Along this path, Arguello et al. (2022a, 2022b, 2023) utilized a multiphysics phase-field approach coupled with open-source finite element software to simulate dendrite nucleation and growth in lithium-metal batteries, incorporating detailed electrochemical reaction kinetics and ionic transport. Similarly, Hong and Viswanathan (2018) developed a phase-field model that includes Butler-Volmer charge transfer kinetics and non-ideal electrolyte behavior, enabling prediction of lithium dendrite morphologies with good agreement to experiments. Chen et al. (2015) proposed a nonlinear phase-field model that accounts for anisotropic surface energy and overpotential effects to describe electrodeposition patterns. Liang et al. (2012) integrated phase-field modeling with electrochemical interface evolution, providing a comprehensive description of the electrode-electrolyte interface. Recent contributions have further expanded this framework: Qi et al. developed a three-dimensional multiphysics model (Qi et al., 2024) and an electrochemical-mechanical coupled approach for solid-state batteries (Qi et al., 2025), while Liu et al. (2021) integrated atomistic calculations of charge transfer physics with a mesoscale phase-field model to reveal how cation desolvation energies dictate the transition from dendritic Li to smooth Mg plating; meanwhile Qiao et al. (2022) provided a quantitative analysis of temperature and pulse charging effects on dendrite inhibition. Additionally, the broader landscape of anode materials and their storage mechanisms has been recently reviewed by Yi et al. (2024).

The above cited models provide useful insights on the electrodeposition of any metal – perhaps with the exception of the case of magnesium, which is less prone to dendrite formation (Li, 2025) –, where similarly complex morphologies and growth dynamics occur (He et al., 2024; Jian et al., 2024; Yao et al., 2021). However, most of these are highly specific and were mainly developed and validated for lithium-based systems. Moreover, the intricacies of the highly specific case studies, the mathematical complexity of the models, the technicalities of the numerical solvers and the occasional lack of full details are, in fact, hindering reproducibility and usability of phase-field models for electrodeposition. In this context, our work provides a simple, general, physically justified, and easily reproducible framework that simulates the electrodeposition of virtually any metal. Thanks to its simple and general nature, our model aims at constituting a general and computationally friendly platform for the development of more complex and/or bespoke models for metal deposition systems. We based the development of out electrochemical case on the well-assessed model by Kobayashi (1993) developed for metal solidification from a melt. The thermal driving force has been replaced by an electrochemical one, based on the coupling of electrical and chemical generalized forces at the metal-electrolyte interface. This allowed us to manipulate rigorously the electrochemical generalized force incorporating electrical information implicitly. We present the formulation of the model along with numerical examples that demonstrate its ability to reproduce key features of dendritic morphologies and their dependence on system variables and operating parameters. The model equations are discretized spatially using classical finite difference schemes and written in matrix form to optimize computational times (D'Autilia et al., 2020). For time integration, we employ the explicit Euler method being implementation-friendly. We provide full numerical details to ensure the reproducibility of our results. More advanced and efficient time discretization techniques will be explored in future work. However, the focus of this paper is primarily on presenting and experimentally validating the model.

Screening numerical tests were performed to select appropriate domain size, spatial and temporal resolution in order to successfully capture dendritic structures. Then, we carried out a quantitative assessment of the formed dendrites; to this end we employ numerical indicators including fractal dimension, skeleton analysis (including metrics such as branch length, number of main branches, endpoints, and connectivity), and the isoperimetric quotient. The fractal dimension and the isoperimetric quotient were employed to characterize dendritic morphologies in various materials, such as Al-Si alloys (Chen et al., 2015; Genau et al., 2013; Ohsasa et al., 2015; Warriner et al., 2020). In this work, we also employ the skeleton-based analysis to provide further insights into the complexity and growth dynamics of dendrites.

Subsequently, we perform parametric studies to explore the impact of model parameters on dendrite morphology and on the occurrence or suppression of dendrite formation. The numerical indicators provide a consistent framework to compare these effects, offering insights into how parameter variations impact dendritic growth patterns. Our results clearly demonstrate that these metrics effectively capture morphological changes in the simulated dendrites, enabling systematic and quantitative comparisons with related experimental and computational studies.

The subsequent sections of this paper is organized as follows. Section 2 introduces the mathematical formulation of the proposed electrochemical phase-field model, derived as restatement of the classical Kobayashi model formalism in the case of an electrochemical driving force, rather than a thermal one. Section 3 details the spatial and temporal discretization strategies. In Section 4, we present numerical simulations and parametric studies investigating the influence of key model parameters on dendritic

morphology. Throughout this analysis, qualitative comparisons between simulated patterns and experimental images are carried out to assess the ability of the model to reproduce the main morphological features observed in electrodeposited dendrites. Section 5 is then devoted to a quantitative characterization of the simulated structures, where several morphological indicators are introduced, including the fractal dimension, skeleton-based metrics, and the inverse isoperimetric quotient. In this section, we also analyze how dendritic morphology evolves as two key model parameters are varied. Finally, Section 6 summarizes the main findings and outlines future directions for improving the numerical efficiency of the proposed approach.

2. Mathematical model

2.1. Original phase-field model by Kobayashi (1993)

The dimensionless phase-field model introduced by Kobayashi (1993) provides a minimal and elegant framework for simulating dendritic crystal growth in pure materials. The model is posed on a square two-dimensional spatial domain $\Omega = [0, L] \times [0, L]$ with $L > 0$, where dendritic growth takes place, and a final time $t_f > 0$. The model contains two unknown variables: (i) a phase variable $\phi(x, y, t)$, $(x, y) \in \Omega$, $t \in [0, t_f]$, which smoothly transitions between the solid ($\phi = 1$) and liquid ($\phi = 0$) phases, and (ii) a nondimensional temperature field $T(x, y, t)$, $(x, y) \in \Omega$, $t \in [0, t_f]$, which governs the thermodynamic driving force for phase change. The evolution of the phase field $\phi(x, y, t)$ is derived from a Ginzburg-Landau-type free energy functional incorporating a double-well potential and interfacial energy:

$$\mathcal{F}[\phi, m(T)] = \int_\Omega \left(\frac{1}{2} \varepsilon(\theta(\nabla\phi)) \|\nabla\phi\|^2 + F(\phi, m(T)) \right) \mathrm{d}\mathbf{x} \tag{1}$$

where: $\theta(\nabla\phi) := \operatorname{atan}\left(\frac{\phi_x}{\phi_y}\right)$ denotes the angle between the interface normal and the x-direction,

$$\varepsilon(\theta) := \varepsilon_0 \left[1 + \delta \cos(j(\theta - \theta_0))\right] \tag{2}$$

is the surface energy anisotropy,

$$m(T) := \frac{\alpha}{\pi} \operatorname{atan}\left[\gamma(T_{eq} - T)\right] \tag{3}$$

is the driving force and

$$F(\phi, m) := \phi(1 - \phi)\left(\phi - \frac{1}{2} + m\right) \tag{4}$$

is a double-well potential. In (2)–(3), θ_0 is the initial offset angle and taken as a constant, δ is the strength of the anisotropy, ε_0 is the mean value of ε, j is the mode number of anisotropy. In (4), $m \in \left(-\frac{1}{2}, \frac{1}{2}\right)$ is a parameter that tunes the distance between the two minima of $F(\phi, m)$. The equation for T stems from conservation of enthalpy (Kobayashi, 1993).

The governing equations are thus:

$$\begin{cases} \tau \frac{\partial\phi}{\partial t} = -\frac{\partial}{\partial x}\left(\varepsilon\varepsilon' \frac{\partial\phi}{\partial y}\right) + \frac{\partial}{\partial y}\left(\varepsilon\varepsilon' \frac{\partial\phi}{\partial x}\right) + \nabla \cdot \left(\varepsilon^2(\theta)\nabla\phi\right) + \phi(1 - \phi)\left(\phi - \frac{1}{2} + m(T)\right); \\ \frac{\partial T}{\partial t} = \nabla^2 T + K \frac{\partial\phi}{\partial t}, \end{cases} \tag{5}$$

where $\tau > 0$ is a suitable time scaling constant, $K > 0$ is a dimensionless latent heat parameter and $\varepsilon'(\theta) = -j\delta\varepsilon_0 \sin(j(\theta - \theta_0))$ is the derivative of $\varepsilon(\theta)$ w.r.t. θ. The system (5) is completed by homogeneous Neumann boundary conditions:

$$\nabla\phi \cdot \mathbf{n} = \nabla T \cdot \mathbf{n} = 0, \qquad (x, y) \in \partial\Omega, \quad t \in [0, t_f], \tag{6}$$

where $\mathbf{n} : \partial\Omega \to \mathbb{R}^2$ is the unit outward vector field on $\partial\Omega$. The initial condition is

$$\phi(x, y, 0) = \begin{cases} 1 & \text{if} \quad (x, y) \in S; \\ 0 & \text{if} \quad (x, y) \in \Omega \setminus S, \end{cases} \qquad T(x, y, 0) = \begin{cases} 0 & \text{if} \quad (x, y) \in S; \\ 1 & \text{if} \quad (x, y) \in \Omega \setminus S, \end{cases} \tag{7}$$

where $S \subset \Omega$ is the initial nucleation site and can be chosen arbitrarily. This model captures the essential features of dendritic pattern formation, including the role of anisotropy and interfacial kinetics, and has been widely used as a benchmark for studying solidification phenomena in two dimensions (Biner, 2017).

2.2. Phase-field model for dendritic growth in electrodeposition

The model proposed in this paper extends the classic phase-field formulation by Kobayashi (1993) reported in Section 2.1 to describe dendritic growth under electrochemical conditions, such as those encountered in electrodeposition processes. A central modification is the replacement of the thermal field equation (second equation in (5)) with a mass transport equation for the dimensionless concentration of the electroactive species, $u(x, y, t)$, thereby reflecting the consumption of ionic species due to the electrode reaction responsible for solid phase formation. The new system thus consists of two coupled equations: one describing the evolution of the phase-field variable $\phi(x, y, t)$, and the other governing the dynamics of the electroactive species concentration $u(x, y, t)$, both for $(x, y) \in \Omega := [0, L] \times [0, L] \subset \mathbb{R}^2$, and $t \in [0, t_f]$. For ease of presentation, we will first present the derivation of the equation for $u(x, y, t)$.

2.2.1. Derivation of the mass transport equation

In the original formulation (5), the dimensionless temperature field $T(x, y, t)$ provided the driving force for phase transformation. In the present electrochemical context, the second equation in (5) is replaced by a mass transport equation for the *dimensionless* concentration $u(x, y, t)$ of the electroactive species. To this end, let $C(x, y, t)\left[\frac{\text{mol}}{\text{m}^3}\right]$ be its corresponding *dimensional* concentration. Since the ionic species $C(x, y, t)$ undergoes reduction at the interface, its evolution is governed by the following reaction-diffusion equation:

$$\frac{\partial C}{\partial t} = D_C \nabla^2 C - R(\phi, \nabla\phi, \partial\phi/\partial t), \tag{8}$$

where $D_C > 0\left[\frac{\text{m}^2}{\text{s}}\right]$ is the dimensional diffusion coefficient of the electroactive species $C(x, y, t)$, and

$$R(\phi, \nabla\phi, \partial\phi/\partial t) := \frac{\kappa \frac{\partial\phi}{\partial t} \frac{i_L}{zF} \|\nabla\phi\|}{\kappa \frac{\partial\phi}{\partial t} + \frac{i_L}{zF}\|\nabla\phi\|} = \frac{\kappa \frac{\partial\phi}{\partial t}\|\nabla\phi\|}{\kappa \frac{zF}{i_L}\frac{\partial\phi}{\partial t} + \|\nabla\phi\|} \tag{9}$$

is a nonlinear reaction term representing the local consumption of species due to the electrochemical reaction that forms the phase, where $\kappa\left[\frac{\text{mol}}{\text{m}^3}\right]$ is the molar density of the metal, $i_L\left[\frac{\text{C}}{\text{m}^2\text{s}}\right]$ is the current density, $F\left[\frac{\text{C}}{\text{eq}}\right]$ is the Faraday constant, $z\left[\frac{\text{eq}}{\text{mol}}\right]$ is the valency of the electroactive species and $\|\cdot\|$ indicates the Euclidean norm. The term (9) is defined to account for both kinetically controlled and mass-transport-limited regimes, as follows. The consumption of C is assumed to be directly proportional to the rate of phase transformation, $\partial\phi/\partial t$, in the limit of fast ion transport. However, in regimes where mass transport becomes rate-limiting, the maximum consumption rate is constrained by the limiting current density i_L. To convert this surface-based current limit into a volumetric source term, the active reaction region is identified with the diffuse interface, where $\nabla\phi$ is finite. Thus, the sink term $R(\phi, \nabla\phi, \partial\phi/\partial t)$ defined in (9) interpolates between two limiting cases:

- For $\kappa\,\partial\phi/\partial t \ll zFi_L$, the consumption rate is proportional to $\kappa\,\partial\phi/\partial t$.
- For $\kappa\,\partial\phi/\partial t \gg zFi_L$, the consumption saturates at zFi_L, reflecting the transport limitation.

The regularized formulation (9) ensures a smooth transition between kinetic and transport-controlled growth regimes, while preserving the consistency of the model with physical constraints. We now adimensionalize Eq. (8). To this end, we introduce the *dimensionless* concentration variable $u = u(x, y, t)$ defined as follows:

$$u(x, y, t) = \frac{C(x, y, t)}{C_0}, \tag{10}$$

where $C_0\left[\frac{\text{mol}}{\text{m}^3}\right]$ is the dimensional bulk concentration. We adimensionalize time as follows:

$$t = t_0\widetilde{t}, \tag{11}$$

where $\widetilde{t}$ is the dimensionless time and t_0 [s] is the characteristic time of the process. Moreover, we adimensionalize space as follows:

$$(x, y) = L_0(\widetilde{x}, \widetilde{y}), \tag{12}$$

where $(\widetilde{x}, \widetilde{y})$ are the *dimensionless* space variables and L_0 [m] is the characteristic length of the process. By substituting (10), (11) and (12) in (8) we obtain

$$\frac{C_0}{t_0}\frac{\partial u}{\partial \widetilde{t}} = \frac{C_0 D_C}{L_0^2}\widetilde{\nabla}^2 u - \frac{\frac{\kappa}{t_0 L_0}\frac{\partial\phi}{\partial \widetilde{t}}\|\widetilde{\nabla}\phi\|}{\frac{\kappa z F}{t_0 i_L}\frac{\partial\phi}{\partial \widetilde{t}} + \frac{1}{L_0}\|\widetilde{\nabla}\phi\|}, \tag{13}$$

where $\widetilde{\nabla}$ is the dimensionless spatial gradient, i.e. the gradient w.r.t. $(\widetilde{x}, \widetilde{y})$. By multiplying both sides of (13) by $\frac{t_0}{C_0}$ we obtain the following dimensionless mass transport equation:

$$\frac{\partial u}{\partial \widetilde{t}} = d_u\widetilde{\nabla}^2 u - \frac{\widetilde{\kappa}\frac{\partial\phi}{\partial \widetilde{t}}\|\widetilde{\nabla}\phi\|}{\frac{1}{\widetilde{i}_L}\frac{\partial\phi}{\partial \widetilde{t}} + \|\widetilde{\nabla}\phi\|}, \tag{14}$$

where $d_u := \frac{t_0 D_C}{L_0^2}$, $\widetilde{\kappa} := \frac{\kappa\xi}{C_0}$, and $\widetilde{i}_L := \frac{t_0 i_L}{\kappa z F L_0}$.

2.2.2. Derivation of the phase-field equation

The equation for the evolution of ϕ (first equation of (5), already in dimensionless form) is slightly modified as follows:

$$\tau\frac{\partial\phi}{\partial t} = -\frac{\partial}{\partial x}\left(\varepsilon\varepsilon'\frac{\partial\phi}{\partial y}\right) + \frac{\partial}{\partial y}\left(\varepsilon\varepsilon'\frac{\partial\phi}{\partial x}\right) + d_\phi\nabla\cdot(\varepsilon^2(\theta)\nabla\phi) + \phi(1-\phi)\left(\phi - \frac{1}{2} + m(u)\right). \tag{15}$$

The difference between the first equation in (5) and (15) is in the electrochemical driving force $m(u)$ defined as follows:

$$m(u) = \frac{\alpha}{\pi}\,\text{atan}\left[\widetilde{\gamma}\left(u - u_{\text{nucl}}\right)\right], \tag{16}$$

where $u_{\text{nucl}} > 0$ is the dimensionless equilibrium concentration and $\alpha \in (0,1)$ and $\widetilde{\gamma} > 0$ are two tunable parameters weighting the driving force, where $u = u_{\text{nucl}}$, $u > u_{\text{nucl}}$ and $u < u_{\text{nucl}}$ represent the Nernstian, the plating and the stripping conditions, respectively. The driving force (16) is expressed through Kobayashi's formalism (5), deriving its specific implementation from electrochemical principles. We now thus present the derivation of (16). In classical phase-field models for solidification, the thermodynamic driving force for the evolution of the phase field is often represented by a temperature imbalance between the current state and the equilibrium state. Instead, in the context of electrochemical processes such as electrodeposition, the appropriate driving force is the overvoltage η, which accounts for the deviation of the local electrochemical potential from equilibrium conditions. As a result of the electrochemical coupling, the overvoltage (in dimensional form) can be expressed with a local Nernst equation for the local concentration at the electrode/electrolyte interface:

$$\eta(x,y,t) = \frac{RT}{zF} \ln\left(\frac{C(x,y,t)}{C_0}\right), \tag{17}$$

where $C_0 > 0 \left[\frac{\text{mol}}{\text{m}^3}\right]$ is the dimensional bulk concentration of the electroactive species. In the case of electrochemical phase formation, a nucleation overvoltage η_{nucl} is required in addition to the charge-transfer contribution (Popov et al., 2002). The effective electrochemical driving force is thus $\eta - \eta_{\text{nucl}}$. The phase-field model uses a smoothed electrochemical driving force for the phase transformation, denoted here by $m(\eta)$. This function must be bounded and monotonic in $\eta - \eta_{\text{nucl}}$, and is commonly (Arguello et al., 2022a, 2022b, 2023; Kobayashi, 1993) formulated using an arctangent function:

$$m(\eta) = \frac{\alpha}{\pi} \operatorname{atan}\left[\gamma\left(\eta - \eta_{\text{nucl}}\right)\right], \tag{18}$$

with $\gamma > 0$ being a tunable parameter. The arctangent ensures that $m(\eta)$ is bounded and smoothly saturates at large positive or negative values of η improving numerical stability and physical realism. Substituting (17) in (18) we obtain:

$$m(C) = \frac{\alpha}{\pi} \operatorname{atan}\left[\gamma \frac{RT}{zF} \ln\left(\frac{C}{C_{\text{nucl}}}\right)\right], \tag{19}$$

being, of course, $\eta_{\text{nucl}} = \eta(C_{\text{nucl}}) = \frac{RT}{zF} \ln\left(\frac{C_{\text{nucl}}}{C_0}\right)$ thanks to (17), with C_{nucl} the electroactive species concentration in the electrolyte in equilibrium with the equilibrium nucleus. By using the first-order Taylor expansion $\ln(x+1) = x + o(x)$ with $x = \frac{C}{C_{\text{nucl}}} - 1$ in (19) we obtain the following electrochemical driving force as a function of the dimensional concentration $C(x,y,t)$:

$$m(C) = \frac{\alpha}{\pi} \operatorname{atan}\left[\gamma \frac{RT}{zF}\left(\frac{C}{C_{\text{nucl}}} - 1\right)\right] = \frac{\alpha}{\pi} \operatorname{atan}\left[\gamma \frac{RTC_0}{zFC_{\text{nucl}}}\left(\frac{C}{C_0} - \frac{C_{\text{nucl}}}{C_0}\right)\right]. \tag{20}$$

Using (10) in (20) we obtain the driving force expressed as a function of the dimensionless concentration $u(x,y,t)$:

$$m(u) = \frac{\alpha}{\pi} \operatorname{atan}\left[\gamma \frac{RTC_0}{zFC_{\text{nucl}}}\left(u - u_{\text{nucl}}\right)\right] = \frac{\alpha}{\pi} \operatorname{atan}\left[\widetilde{\gamma}\left(u - u_{\text{nucl}}\right)\right], \tag{21}$$

where $\widetilde{\gamma} := \frac{\gamma RTC_0}{zFC_{\text{nucl}}}$, which proves (16).

2.2.3. The full model

We are now in a position to state the full model in dimensionless form, governing the coupled evolution of ϕ and u. For ease of presentation, the $\sim$ notation will be omitted in the remainder of the paper. Therefore, the complete dimensionless model for electrochemical dendrite formation is given by:

$$\begin{cases} \tau \dfrac{\partial \phi}{\partial t} = -\dfrac{\partial}{\partial x}\left(\varepsilon\varepsilon' \dfrac{\partial \phi}{\partial y}\right) + \dfrac{\partial}{\partial y}\left(\varepsilon\varepsilon' \dfrac{\partial \phi}{\partial x}\right) + d_\phi \nabla \cdot \left(\varepsilon^2(\theta)\nabla\phi\right) + \phi(1-\phi)\left(\phi - \dfrac{1}{2} + m(u)\right); \\ \dfrac{\partial u}{\partial t} = d_u \nabla^2 u - \dfrac{\kappa \frac{\partial \phi}{\partial t} \|\nabla\phi\|}{\frac{1}{i_L}\frac{\partial \phi}{\partial t} + \|\nabla\phi\|}, \end{cases} \tag{22}$$

for $(x,y) \in \Omega = [0,L]^2$ and $t \in [0,t_f]$ with ε defined in (2) and $m(u)$ defined in (16). Following Arguello et al. (2022a, 2022b, 2023), we impose the following boundary conditions:

$$\begin{cases} \frac{\partial \phi}{\partial y}(x,0,t) = \frac{\partial u}{\partial y}(x,0,t) = 0, & x \in [0,L]; \\ \frac{\partial \phi}{\partial y}(x,L,t) = \frac{\partial u}{\partial y}(x,L,t) = 0, & x \in [0,L]; \\ \phi(L,y,t) = 0, & y \in [0,L]; \\ u(L,y,t) = 1, & y \in [0,L]; \\ \phi(0,y,t) = 0, & y \in [0,L] \setminus \left[\frac{L}{2} - r, \frac{L}{2} + r\right]; \\ \phi(0,y,t) = 1, & y \in \left[\frac{L}{2} - r, \frac{L}{2} + r\right]; \\ u(0,y,t) = 1, & y \in [0,L] \setminus \left[\frac{L}{2} - r, \frac{L}{2} + r\right]; \\ u(0,y,t) = 0, & y \in \left[\frac{L}{2} - r, \frac{L}{2} + r\right], \end{cases} \tag{23}$$

for $t \in [0, t_f]$, where $r > 0$. The initial condition is:

$$\phi_0(x,y) = \begin{cases} 1, & (x,y) \in S; \\ 0, & (x,y) \in \Omega \setminus S, \end{cases} \qquad u_0(x,y) = \begin{cases} 0, & (x,y) \in S; \\ u_0 = 1, & (x,y) \in \Omega \setminus S, \end{cases} \tag{24}$$

where S is the right half-circle of radius r centered at $\left(0, \frac{L}{2}\right)$:

$$S := \left\{ (x,y) \in \Omega \ : \ x \geq 0, \ x^2 + \left(y - \frac{L}{2}\right)^2 \leq r^2 \right\}. \tag{25}$$

Physically, the boundary conditions (23) and the initial conditions (24) entail that the initial nucleation site is the half-circle S defined in (25), see Fig. 1 in Section 4.1. To ensure that the initial condition (24) fulfills the Nernstian condition $u > u_{\text{nucl}}$, we choose $u_{\text{nucl}} < u_0 = 1$. In the case of metal plating in the presence of an SEI that typically contains oxidation products generated by the previous discharge cycle, a reasonable value for the activity coefficient u_{nucl} in can be taken to be 0.2. This choice is also justified by the systematic exploration in Appendix C.

3. Numerical approximation

The PDE model (22) presented in the previous section consists of two coupled equations defined on a square spatial domain. The spatial domain is discretized using a uniform grid with N points in each spatial direction, leading to a total of $N \times N$ grid points $\mathbf{x}_{ij} = (x_j, y_i) := ((j-1)h, (i-1)h)$, $i, j = 1, \dots, N$ and $h := \frac{L}{N-1}$ is the grid size. Spatial derivatives are approximated using second-order central finite differences, which provide the discretization of the Laplacian, the mixed derivatives, and the first-order operators appearing in the anisotropic term. The spatially discretized solution consists of two time-dependent matrix-valued functions $\boldsymbol{\Phi}, U : [0, t_f] \to \mathbb{R}^{(N-2)\times(N-2)}$, where $\boldsymbol{\Phi}_{ij}(t) \approx \phi(x_j, y_i, t)$ and $U_{ij}(t) \approx u(x_j, y_i, t)$ for all $i, j = 2, \dots, N-1$, and $\boldsymbol{\Phi}_{ij}(0) = \phi_0(x_j, y_i)$, $U_{ij}(0) = u_0(x_j, y_i)$ for all $i, j = 2, \dots, N-1$, where the initial data ϕ_0 and u_0 are defined in (24). Therefore, $\boldsymbol{\Phi}$ and U approximate ϕ and u at the interior spatial nodes. This procedure yields the following semi-discrete system of matrix-valued ordinary differential equations (ODEs):

$$\begin{cases} \tau \dfrac{d\boldsymbol{\Phi}(t)}{dt} = \mathcal{F}_{\boldsymbol{\Phi}}(\boldsymbol{\Phi}(t), U(t)); \\ \dfrac{dU(t)}{dt} = \mathcal{F}_U(\boldsymbol{\Phi}(t), U(t)), \end{cases} \qquad t \in [0, t_f]. \tag{26}$$

The operators $\mathcal{F}_{\boldsymbol{\Phi}}$ and $\mathcal{F}_U$ incorporate all discretized spatial contributions – diffusion, mixed derivatives, nonlinear reaction terms – together with the imposed mixed boundary conditions (23). Time integration is carried out adopting the explicit Euler method, which updates the solution as

$$\begin{cases} \boldsymbol{\Phi}^{n+1} = \boldsymbol{\Phi}^n + \frac{\Delta t}{\tau} \mathcal{F}_{\boldsymbol{\Phi}}(\boldsymbol{\Phi}^n, U^n); \\ U^{n+1} = U^n + \Delta t \, \mathcal{F}_U(\boldsymbol{\Phi}^n, U^n), \end{cases} \tag{27}$$

where Δt is the time step and the superscript n denotes the discrete time level $t_n := n\Delta t$, for $n = 0, \dots, N_T - 1$, where $N_T := \left\lceil \frac{t_f}{\Delta t} \right\rceil$. The iteration (27) is initialized with $\boldsymbol{\Phi}^0 = \boldsymbol{\Phi}(0)$, $U^0 = U(0)$. This yields a fully discrete reaction-diffusion system whose detailed operator structure $\mathcal{F}_{\boldsymbol{\Phi}}$ and $\mathcal{F}_U$ is presented in Appendix A.

4. Numerical simulations

This section presents numerical simulations of the electrochemical model. Unless otherwise specified, all model and numerical parameters are fixed as reported in Table 1, while the varying parameters are explicitly indicated for each test to generate different dendritic structures. Preliminary numerical studies were carried out to evaluate the effect of the computational domain size L, the grid resolution N and the time step Δt. The results showed that when the domain is too large or the spatial resolution too coarse, the dendritic structures are not suitably approximated. For this reason, we employ a very fine spatial grid and we fixed $L = 10$ and $N = 250$ for all simulations. This, in turn, supports the choice of an explicit time solver, which requires reasonable execution times and memory occupation, compared to implicit solvers. Moreover, the time step Δt = 1e-4 was chosen in order to ensure the stability of the numerical method. In the initial condition (24), the radius of the initial spot is set to $r = 0.25$, chosen to ensure a sufficiently large seed for the development of the dendritic structure. This configuration is illustrated in Fig. 1. The choice of $u_{\text{nucl}} = 0.2$ is discussed in Appendix C.

4.1. Numerical tests to assess dendrite growth under physical parameters variation

In this set of numerical experiments, we systematically investigate how variations in selected physical parameters affect the morphology and growth dynamics of dendritic structures. The parameters considered are:

- *anisotropy mode number* j, which controls the number of preferential growth directions;
- *kinetic coefficient* κ, which modulates the rate at which the concentration field u adapts to the moving interface;
- *dimensionless current density* i_L, which modulates the strength of the flux term and effectively influences the growth rate.

Table 1
Parameters used in the dimensionless model (22)–(24) for all the simulations, unless otherwise specified.

Category	Parameter	Value
Model parameters	τ	0.0003
	ϵ_0	0.01
	δ	0.05
	d_ϕ	1
	d_u	1
	α	0.9
	u_{nucl}	0.2
	γ	10
	θ_0	0.2
Parameters varied in simulations	j	4, 6, 8
	κ	1.2, 1.4, 1.6
	i_L	30, 40, 50

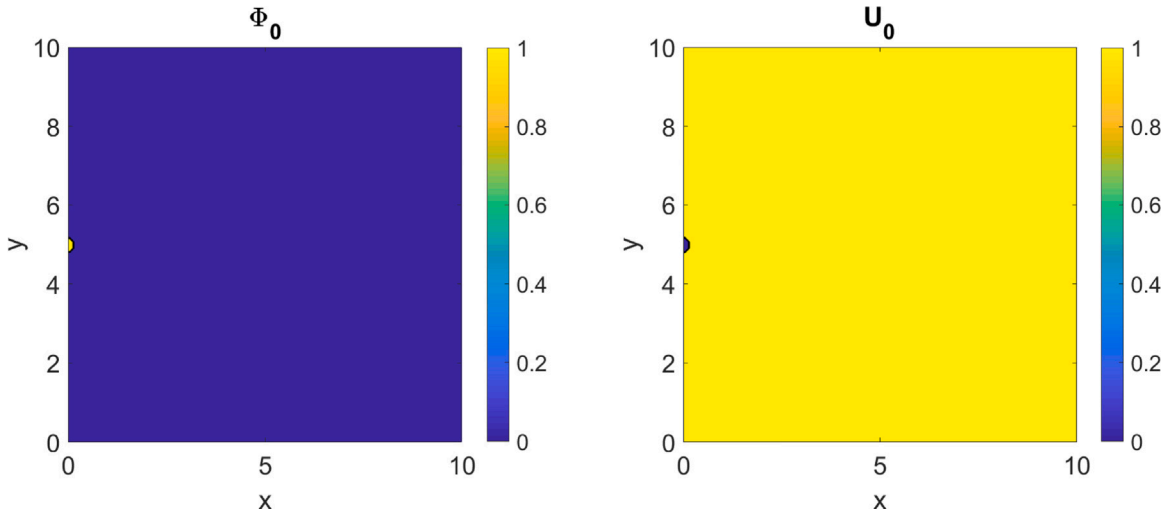

Fig. 1. Initial condition for all simulations. Left: phase-field variable ϕ. Right: concentration field u. Both fields show a circular seed located at the center of the left-hand boundary.

The final simulation time t_f is defined as the time when the dendrite reaches the right-hand boundary of the computational domain. Tables 2a–2c report the corresponding t_f for each parameter variation, providing a quantitative measure of the growth speed and dynamics. For each Test we show a figure containing the numerical simulations alongside their corresponding experimental images to support the numerical findings. The discussion of the experimental comparisons is presented at the end of this section.

Test 1: Effect of the anisotropy. We first explore the influence of the anisotropy mode number j, fixing the kinetic coefficient at $\kappa = 1.4$ and the dimensionless current at $i_L = 40$. We consider $j = 4, 6, 8$. It is well known that the parameter j controls the anisotropy of the dendrite, determining the preferred growth directions and the branching patterns. In particular, we expect that higher values of j lead to a larger number of main branches, resulting in thinner and more ramified structures, whereas lower values produce dendrites with fewer, thicker, and less branched arms. In this Test we verify this behavior within our model (22)–(23). Fig. 2(a) illustrates the phase-field variable ϕ at the corresponding final simulation times. Since the concentration field u is the new variable introduced in the electrochemical model (22) we plot its spatial distribution in these simulations to better illustrate its role in the coupled dynamics. We present the concentration u only for this Test because in the subsequent Tests we will focus on the phase-field morphology ϕ, which is the key quantity for identifying and comparing dendritic growth patterns with experiments. Accordingly, in Fig. 2(a) the first row shows the corresponding concentration u for each value $j = 4, 6, 8$, while the second row displays the phase-field variable ϕ.

We observe that the concentration u closely matches the geometry of the corresponding dendrite. In fact, $u \approx 1$ in the bulk of the electrolyte region where the concentration electroactive species is not affected by the electrochemical reaction, but only by diffusion towards the electrode-electrolyte interface, whereas it is depleted to $u \approx 0$ within the growing dendrite, where the material is deposited and consequently the electrolyte is expelled from the domain. This behavior confirms the expected coupling between the concentration field and the phase-field dynamics.

We also observe that a lower value of j (4) produces dendrites with fewer, thicker branches and a relatively faster growth to the boundary. Increasing j to 6 and 8 results in a larger number of thinner branches, creating more branched structures. The final

Table 2
Final simulation time t_f for different anisotropy mode numbers j ($\kappa = 1.4$, $i_L = 40$) in Table (a), for different values of κ ($j = 6$, $i_L = 40$) in Table (b) and for different dimensionless current densities i_L ($j = 6$, $\kappa = 1.4$) in Table (c).

j	Final time t_f
4	0.80
6	0.95
8	1.18

(a)

κ	Final time t_f
1.2	0.78
1.4	0.95
1.6	1.27

(b)

i_L	Final time t_f
30	0.85
40	0.95
50	1.03

(c)

simulation time t_f, collected in Table 2a, increases with j, reflecting that more branched dendrites require more time to reach the boundary.

Comparison with experiments: In Fig. 2(b), we report SEM micrographs of electrodeposited Cu films obtained from acidic sulphate solutions under different growth conditions: additive free bath at −500 (left panel, Bozzini et al., 2006b) and −300 (middle panel, Bozzini et al., 2006a) mV vs Ag/AgCl, and JGB-containing bath at 50 mA cm^{-2} (right panel, Bozzini et al., 2007). Full experimental details are reported in the quoted papers. The sequence of panels shows examples of dendrites exhibiting progressively increasing degree of dendrite branching.

Test 2: Effect of the kinetic coefficient. Next, we study the effect of the kinetic coefficient κ, fixing $j = 6$ and $i_L = 40$. We consider three representative values: $\kappa = 1.2$, 1.4, and 1.6. Fig. 3(a) shows the dendritic structures at the corresponding final times. The final time values are reported in Table 2b. In this case, lower κ (1.2) results in faster growth and longer dendritic arms. Intermediate κ (1.4) produces slightly slower growth but more branched and complex dendrites. Higher κ (1.6) slows growth, yielding shorter and more compact dendrites.

Comparison with experiments: In Fig. 3(b), we show SEM micrographs of Cu (left and right panels) and Ag (middle panel) films, electrodeposited under different conditions: (left panel) additive-free solution at 20 mA cm^{-2} (Bozzini et al., 2007), (right panel) JGB solution at 10 mA cm^{-2} (Bozzini et al., 2007) and (middle panel) cyanide electrolyte at 10 mA cm^{-2} (Caramia & Bozzini, 2015). Full experimental details are reported in the quoted papers. This sequence of images showcases dendrites of similar branching degree, exhibiting branches of different thickness.

Test 3: Effect of the current density. Finally, we analyze the influence of the dimensionless current density i_L, fixing $j = 6$ and $\kappa = 1.4$. We consider $i_L = 30$, 40, and 50. Fig. 4(a) shows the dendritic structures at the final times, whose values are reported in Table 2c. The morphology, in terms of the number and thickness of branches, remains largely unchanged across the tested current densities. The growth speed is slightly modulated by i_L, with higher values slowing down dendritic propagation, resulting in increased final times t_f.

Comparison with experiments: In Fig. 4, we report SEM micrographs at different magnifications of Cu electrodeposited at 5 mA cm^{-2} (Bozzini et al., 2007) in the absence of additives. Full experimental details are reported in the quoted paper. In the simple-salt bath, these galvanostatic conditions yield a highly branched dendritic structure, with main and side features of similar thickness.

These results provide a detailed qualitative picture of how each parameter influences the morphology and dynamics of the dendritic growth. In the following section, some indicators will be introduced to allow a quantitative analysis of the simulated dendrites.

5. Quantitative morphological analysis of dendritic structures

To systematically describe the morphological complexity of the dendritic structures obtained from the numerical simulations, we introduce a set of indicators, given by: (a) Skeleton-based topological measures, (b) the Fractal Dimension (D_f), and (c) the Inverse Isoperimetric Quotient (IIQ). Algorithmic details on their computation are reported in Appendix B. In this Section, first of all we briefly recall their definition and, as an example, we apply them to analyze the simulated dendrites obtained in Test 2 of Section 4 for different values of the kinetic coefficient κ. Secondly, for fixed anisotropy, we consider systematic simulations in the parameter space (κ, i_L) to: (i) describe the appearance or not of dendrites; (ii) to calculate the corresponding map of the IIQ indicator and then (iii) to obtain a segmentation is sub-regions of the parameter space. As final result, we show that three zones can be identified where simulated and experimental dendrites of same features belong.

5.1. Morphological indicators and quantitative analysis for Test 2

(a) Skeleton-based topological measures

The skeleton of each dendritic structure is extracted from the binary image corresponding to a given simulated numerical solution by using MATLAB's `bwmorph` function with the `'skel'` operation. This operation reduces the dendrite shape to a one-pixel-thick medial axis while preserving its connectivity. From the skeleton, the following indicators are computed, as detailed in Appendix B: L_S total Skeleton length, n_B number of Branch points, n_E number of End points, d_B Branch density and m_T Mean tortuosity.

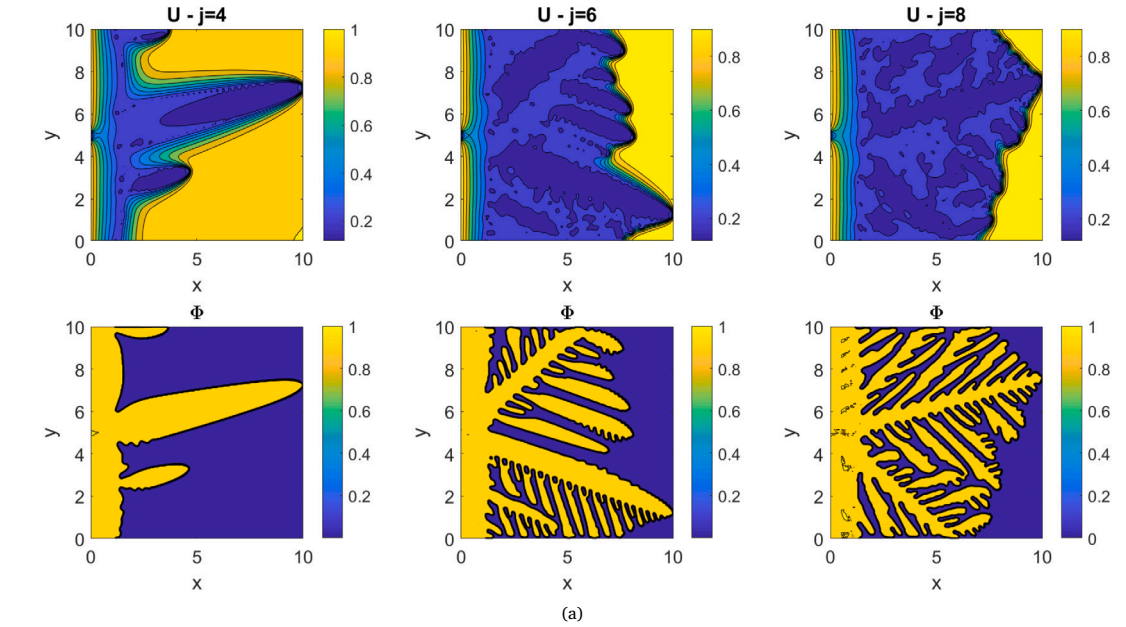

Fig. 2. Test 1: Effect of the anisotropy. (a) Concentration and phase-field variable at the final simulation time for different anisotropy mode numbers j. From left to right: $j = 4$, 6, 8. Increasing j increases the number of thinner branches and produces more ramified dendritic structures, which in turn leads to a larger region where the concentration field is significantly reduced. (b) SEM micrographs of electrodeposited Cu films: additive free acidic sulphate solution at −500 (left panel Bozzini et al., 2006b) and −300 (middle panel Bozzini et al., 2006a) mV vs Ag/AgCl; with added JGB 50 mA cm^{-2} (right panel Bozzini et al., 2007).
Source: Reprinted with permission from Bozzini et al. (2006b, Figure 12), Bozzini et al. (2006a, Figure 13) and Bozzini et al. (2007, Figure 5(h)).

(b) Fractal dimension (D_f)

The Fractal Dimension provides a measure of the spatial complexity and branching irregularity, higher values of D_f indicate more space-filling and ramified structures. D_f is estimated using the *box-counting* algorithm applied to the dendrite interface.

(c) Inverse isoperimetric quotient (IIQ)

The *Inverse Isoperimetric Quotient* is defined as:

$$IIQ = \begin{cases} \dfrac{P^2}{4\pi A} & \text{if } A \neq 0; \\ 0 & \text{if } A = 0, \end{cases} \tag{28}$$

where P is the total perimeter and A is the area covered by the dendrite. IIQ can be used as a dendritic growth index: $IIQ = 1$ corresponds to a circular, compact shape, while higher values indicate increasing branching and morphological irregularity of the shape.

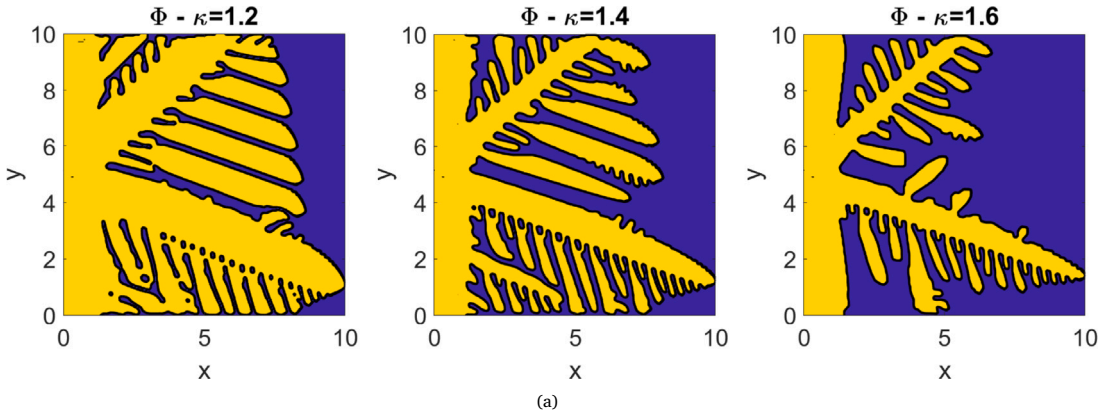

(a)

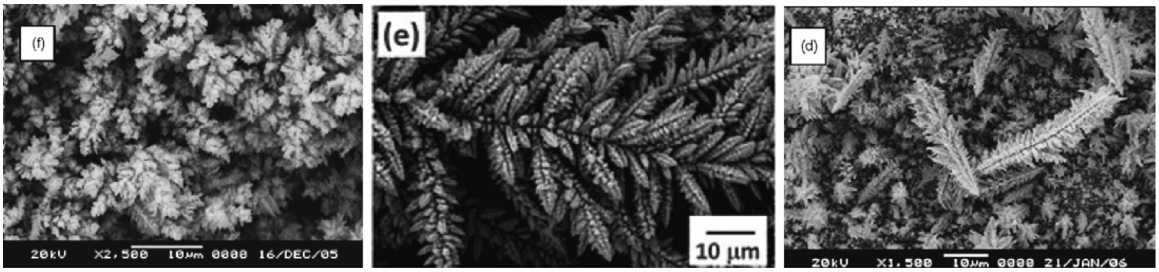

(b)

Fig. 3. Test 2: Effect of the Kinetic Coefficient. (a) Phase-field variable at the final simulation time for different kinetic coefficients κ. From left to right: κ = 1.2, 1.4, 1.6. Lower κ leads to faster and more extended dendritic growth, while higher κ slows growth and produces shorter structures. (b) SEM micrographs of Cu and Ag electrodeposits. (Left panel) Cu, additive-free, 20 mA cm^{-2} (Bozzini et al., 2007); (middle panel) Ag, cyanide electrolyte, 10 mA cm^{-2} (Caramia & Bozzini, 2015). (Right panel) Cu, JGB-containing solution, 10 mA cm^{-2} (Bozzini et al., 2007; Caramia & Bozzini, 2015).
Source: Reprinted with permission from Bozzini et al. (2007, Figure 5(f)), Caramia and Bozzini (2015, Figure 6(e)) and Bozzini et al. (2007, Figure 6(d)).

Table 3
Morphological indicators for increasing kinetic coefficient κ. Skeleton-based metrics are reported in the first five columns.

κ	n_B	n_E	L_S (pixel)	Branch density d_B	Mean tortuosity m_T	D_f	IIQ
1.2	126	79	3362	0.0375	9.605	1.94	31.29
1.4	164	141	3522	0.0466	10.022	1.89	48.32
1.6	104	100	2347	0.0443	6.678	1.81	33.54

As an example, here we analyze the simulations of the phase field variable ϕ obtained for $\kappa = 1.2, 1.4, 1.6$ studied in Test 2 and shown in Fig. 3(a). Fig. 5 shows the level-set contours of ϕ and the corresponding skeletons, highlighting the branching patterns and topological complexity. The calculated morphological indicators summarized in Table 3 reveal that:

- Lower κ (1.2): Dendrites grow relatively fast and directionally, resulting in longer structures with fewer branch points (n_B) and end points (n_E), and moderate total skeleton length (L_S) and branch density (d_B). The mean tortuosity (m_T), fractal dimension (D_f), and inverse isoperimetric quotient (IIQ) indicate intermediate, relatively straight, and compact growth patterns.
- Intermediate κ (1.4): Structures exhibit the most pronounced branching, with the highest number of branch points (n_B) and end points (n_E), the longest total skeleton length (L_S), and maximal branch density (d_B) and mean tortuosity (m_T). Fractal dimension (D_f) and inverse isoperimetric quotient (IIQ) also reach their maximum, reflecting highly intricate and strongly ramified dendritic morphologies.
- Higher κ (1.6): Growth slows down, producing shorter structures with decreased number of branch points (n_B) and end points (n_E). Total skeleton length (L_S), branch density (d_B), mean tortuosity (m_T), fractal dimension (D_f), and inverse isoperimetric quotient (IIQ) all decrease, indicating more compact and less tortuous branching, yet still non-trivial morphologies.

The different morphological indicators considered in this study provide complementary information on dendritic growth, but they are not equally suited for a systematic exploration of the parameter space. The fractal dimension D_f mainly characterizes the space-filling properties of the dendritic structures and reflects their global compactness across scales. Its interpretation, however,

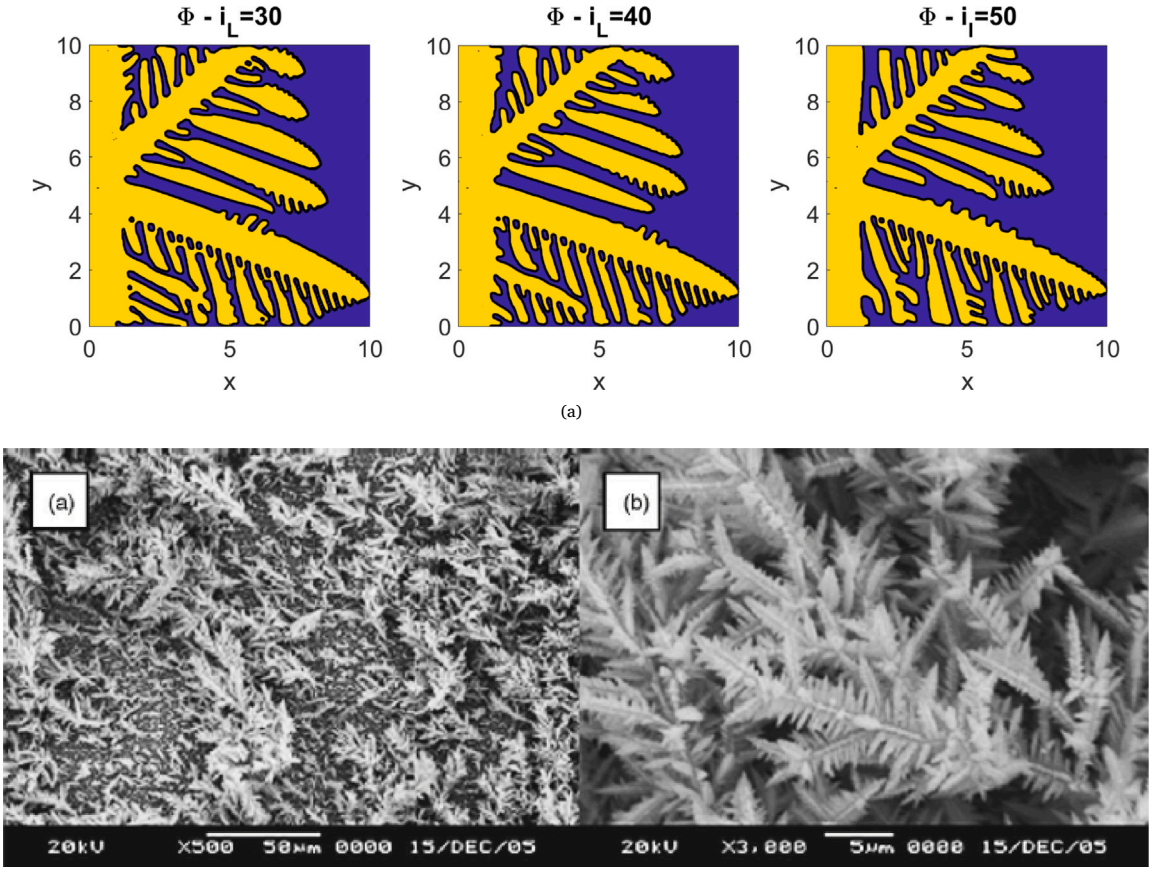

Fig. 4. Test 3: Effect of the Current Density. (a) Phase-field variable at the final simulation time for different dimensionless current densities i_L. From left to right: $i_L = 30$, 40, 50. Morphology remains largely unchanged, while higher i_L slightly slows down growth. (b) SEM micrographs at different magnifications (see figure) of Cu electrodeposited from simple acidic solution at 5 mA cm^{-2} (Bozzini et al., 2007).
Source: Reprinted with permission from Bozzini et al. (2007, Figure 5(a)–(b)).

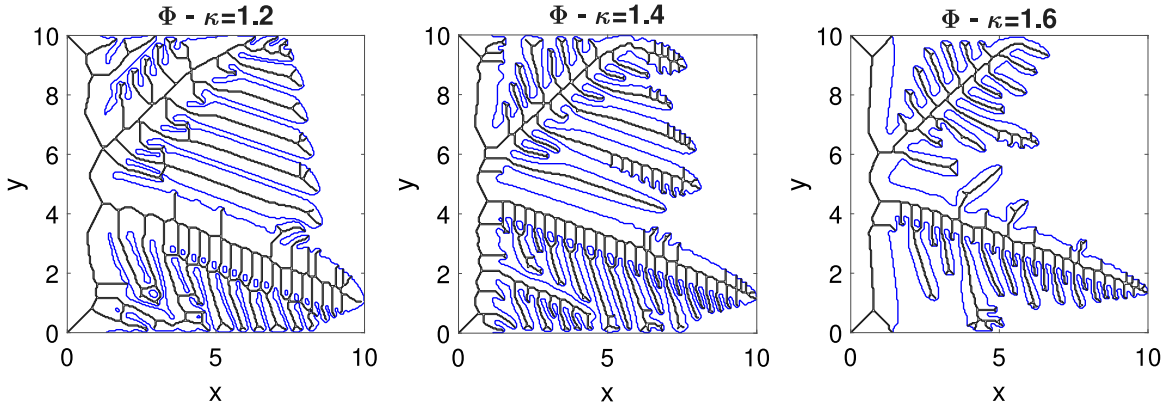

Fig. 5. Morphological analysis of Test 2: Level-set contours (blue) and MATLAB-generated skeletons (black) of the dendritic structures ϕ for $\kappa = 1.2$, 1.4, 1.6. The skeleton highlights the main branches and bifurcations, providing a quantitative view of the morphological complexity.

requires caution, since a clear fractal scaling is not always present over a sufficiently wide range of length scales (Genau et al., 2013). In addition, in Table 3, D_f varies monotonically with the kinetic coefficient κ and therefore does not capture the non-monotonic changes in branching complexity revealed by the skeleton-based indicators. This limits its ability to distinguish between morphologies with similar spatial occupancy but different branching organization.

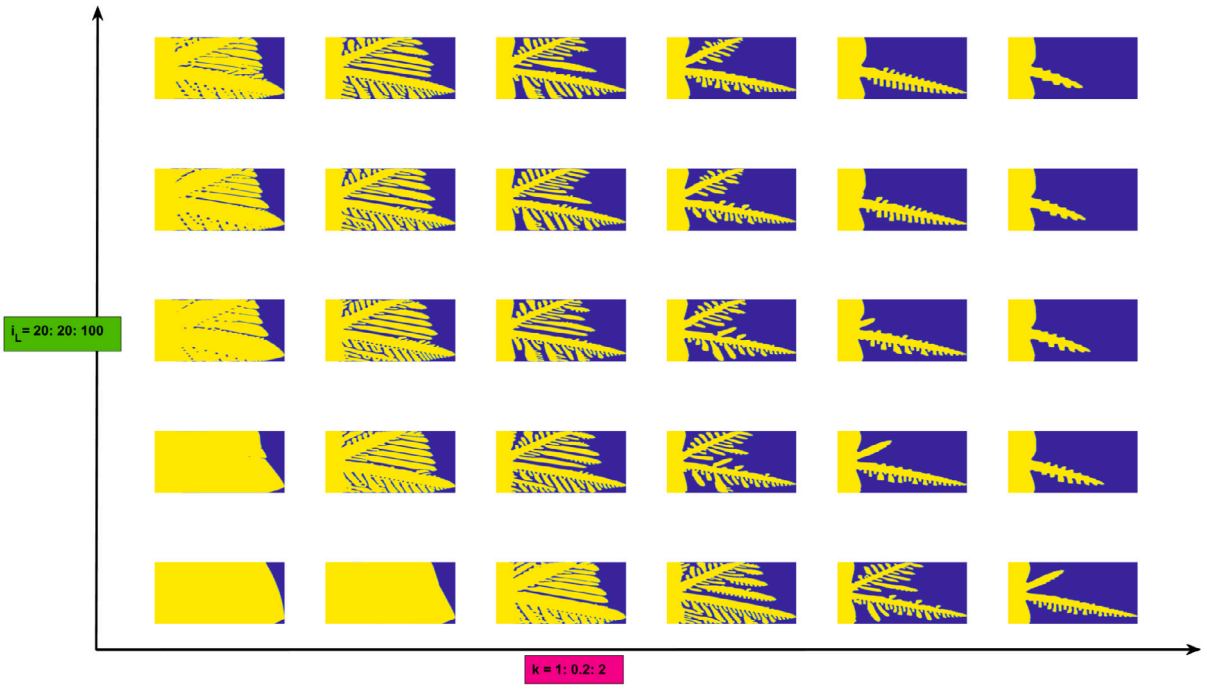

Fig. 6. Phase-field solutions in the parameter space (κ, i_L). Increasingly ramified morphologies appear within a well-defined region of the parameter plane, in agreement with the IIQ-based segmentation in Fig. 7.

Skeleton-based metrics, on the other hand, offer a detailed topological description of the dendritic network, including branching, connectivity, and tortuosity. While highly informative for case-by-case analysis, they rely on multiple descriptors and on post-processing steps that may introduce sensitivity to numerical resolution and algorithmic parameters. Hence, they are less convenient for constructing morphological maps over a wide parameter range.

In contrast, the inverse isoperimetric quotient IIQ provides a single, robust, and scale-independent measure of dendrites, directly linked to spacial development and branching density. By providing a single scalar measure of morphological complexity, it allows for a clear and systematic comparison of different growth regimes. For these reasons, only IIQ is adopted in the following section as descriptor for the exploration of the (κ, i_L) parameter space.

5.2. Morphological analysis in the (κ, i_L) parameter space

In this Section, we fix the anisotropy index $j = 6$ in Eq. (2) and we want to investigate how the dendritic morphologies change in the (κ, i_L) Parameter Space $\mathcal{S}$. Our aim is to use IIQ to analyze the obtained numerical simulations in quantitative way. The main idea is to recognize a segmentation of the above parameter space and identify therein significant morphological classes of dendrites. This is a first attempt towards a systematic quantitative comparisons with experiments, as we will show in the next Subsection.

First of all, we choose a discretization of $\mathcal{S}$, with $\kappa \in [1, 2]$ and $i_L \in [10, 100]$ and we apply systematically our numerical solver to approximate the phase field variable $\phi(x, y)$.

A selection of the numerical simulations obtained is reported in Fig. 6 for some values of the current i_L and kinetic parameter κ in $\mathcal{S}$. This computational results clearly highlights the transition from compact to branched deposits. (For clarity of visualization, the axes are not to scale.) To complete our quantitative analysis we compute the dendritic growth index IIQ defined in (28) for all simulated structures. The obtained map is reported in Fig. 7.

Interpretation of morphological transitions in the (κ, i_L) *space*

Fig. 6 provides a systematic overview of the simulated growth morphologies across the (κ, i_L) parameter space. At low applied current densities ($i_L \lesssim 20$), the deposits remain compact for all explored values of κ. The growth fronts are smooth and only weakly perturbed, exhibiting nearly circular or slightly anisotropic shapes. This behavior indicates a stable growth regime that is largely insensitive to variations in interfacial mobility.

As the current density increases, the morphology becomes progressively more sensitive to the kinetic parameter κ. For intermediate values of i_L, the simulations reveal a marked transition from compact to branched structures as κ increases. In this regime, the growth fronts develop pronounced protrusions that evolve into ramified and dendritic patterns, characterized by multiple competing branches and a highly irregular interface.

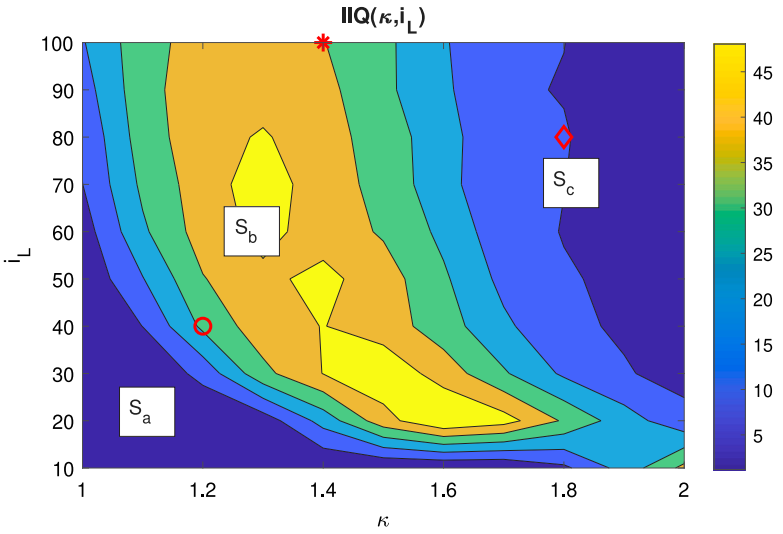

Fig. 7. Segmentation of the parameter space based on the IIQ indicator: region S_a corresponds to $1 \leq \text{IIQ} \leq 1.5$, region S_b corresponds to $\text{IIQ} > 11$, region S_c corresponds to $1.5 < \text{IIQ} \leq 11$. The three highlighted parameter pairs are: $(\kappa, i_L) = (1.2, 40)$, circle located in region S_b; $(\kappa, i_L) = (1.4, 100)$, asterisk located in region S_b; $(\kappa, i_L) = (1.8, 80)$, rhomboid located in region S_c. These three parameter pairs correspond to the numerical simulations in Fig. 8 (right).

At even higher current densities, the morphologies undergo a further qualitative change. Although branching persists, the resulting structures appear more sparse and elongated, with a reduced number of active tips and weaker lateral branching. This suggests that, at large driving forces, growth becomes increasingly dominated by a limited number of advancing branches, leading to rarefied dendritic structures.

Segmentation of the parameter space and comparisons with experiments

Combining a quantitative analysis based on IIQ (Fig. 7) and a qualitative analysis (Fig. 6), the parameter space can be partitioned into three representative morphological classes, highlighted in Fig. 7. These classes are:

- Lower-left region of the parameter space (κ, i_L), called S_a, corresponding to low current densities i_L and low κ. In this region, the IIQ values remain confined to a narrow range close to unity, consistently reflecting the compact and weakly perturbed morphologies with no clear dendritic features observed in the simulations.
- Central region of the parameter space, called S_b, corresponding to higher i_L values compared to S_a. In this region, the IIQ exhibits a strong dependence on κ, with a pronounced increase that signals the onset of morphological instability and the development of highly ramified dendritic structures. Within this class, two distinct growth regimes are observed, namely (i) relatively compact dendritic structures with thick branches, labeled $S_{b(i)}$, and (ii) more open, highly ramified patterns characterized fine branches, labeled $S_{b(ii)}$.
- Right region of the parameter space, called S_c, corresponding to the highest values of both parameters. In this region, the IIQ decreases again, in agreement with the emergence of sparse and rarefied dendrites characterized by a reduced interfacial complexity and dominated by slow dynamics.

Notably, the regions identified through the IIQ analysis (Fig. 7) coincide with those distinguished by direct visual inspection of the simulated morphologies (Fig. 6), confirming that the IIQ captures the essential features of the morphological transitions in the (κ, i_L) space and is therefore an effective metric to discriminate between different growth regimes.

The existence of the morphological classes $S_{b(i)}$, $S_{b(ii)}$ and S_c is backed up experimentally. The left column of Fig. 8 reports a selection of SEM images of Cu electrodeposits, obtained in different conditions from acidic sulphate solutions. Top and middle panels correspond to galvanostatic growth, respectively at 50 mA cm^{-2} from a simple salt solution (Bozzini et al., 2007) and at 20 mA cm^{-2} from a JGB-containing electrolyte (Bozzini et al., 2007), while the bottom panel shows a potentiostatic deposit at −700 mV vs. Ag/AgCl from an additive-free bath (Bozzini et al., 2008). Full experimental details are reported in the quoted papers. The dendrite morphologies found in these electrodeposits exhibit systematic variations in branch length and thickness, that can be associated each to one of the simulated morphological classes of Fig. 8 (right). In conclusion, the results of this section establish a direct link between the model parameters and the experimentally observed growth regimes.

6. Conclusions

In this work, we proposed and numerically investigated a phase-field model for dendritic growth during electrochemical deposition of metal, formulated as a modification of Kobayashi's classical model for thermally-driven dendritic crystal formation

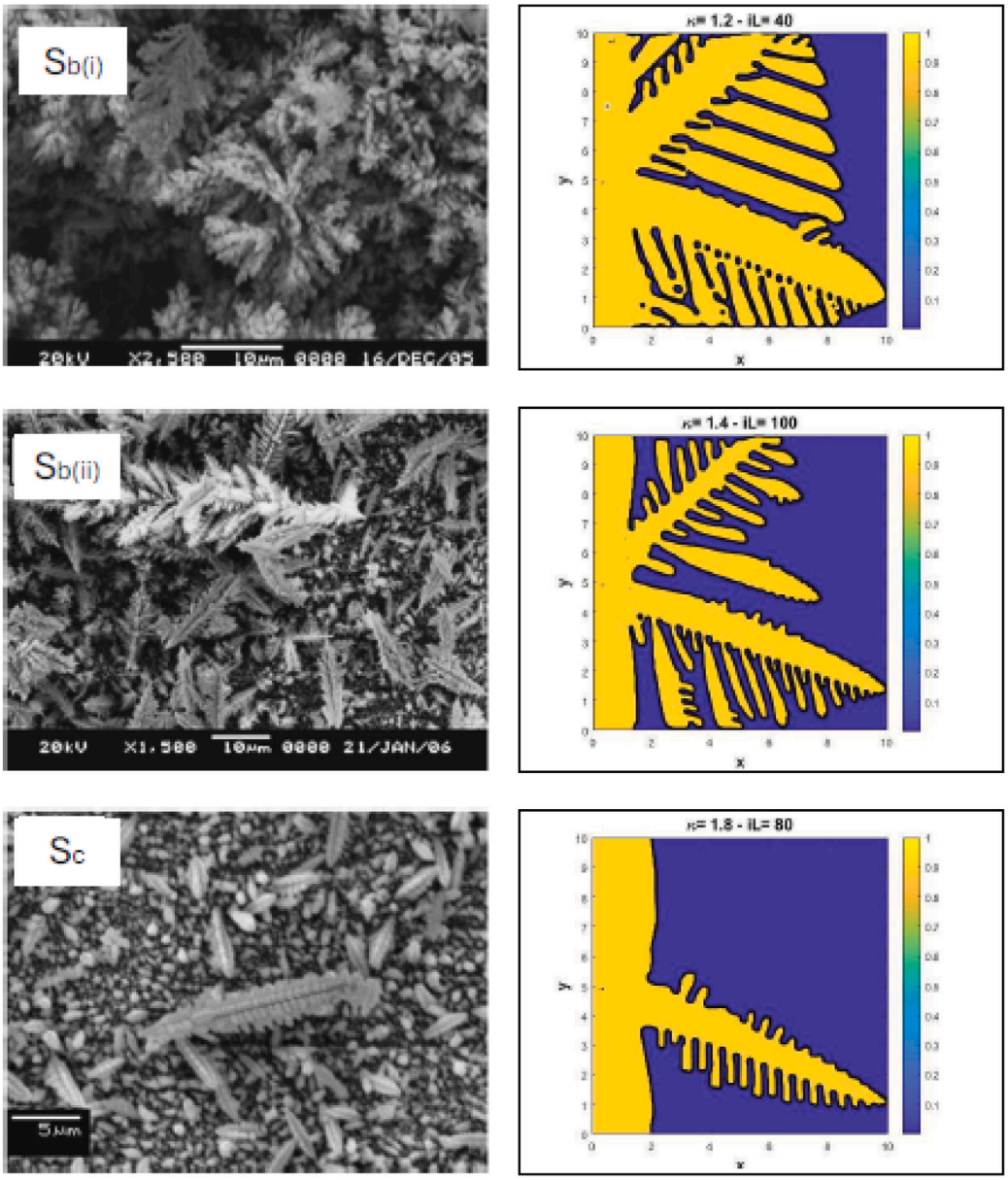

Fig. 8. Comparisons with experiments. $S_{b(i)}$, $S_{b(ii)}$: two representative cases of the S_b region, corresponding to the two distinct strongly ramified dendritic growth regimes observed in the central part of the (κ, i_L) parameter space. S_c: sparse and rarefied growth dominated by a single prevailing branch, representative of the S_c region. The inverse isoperimetric quotient values associated with the three cases are $IIQ = 31.29$, 39.01, and 11.13, respectively. The parameter values (κ, i_L) corresponding to the simulations are highlighted in Fig. 7. The left column shows SEM micrographs of Cu electrodeposits, from acidic sulphate solutions, obtained in the following conditions: (top left panel) additive-free, 50 mA cm^{-2} (Bozzini et al., 2007); (middle left panel) JGB-containing 20 mA cm^{-2} (Bozzini et al., 2007); (bottom left panel) additive-free, −700 mV (Bozzini et al., 2008).
Source: Reprinted with permission from Bozzini et al. (2007, Figure 5(h)–(f)) and Bozzini et al. (2008, Figure 10(c)).

in metal solidification from a melt. By replacing the thermal field with a concentration field and incorporating electrochemical coupling through the local electrochemical potential, the model captures key features of metal electrodeposition dynamics.

Numerical simulations demonstrated that the dendritic morphology is strongly influenced by the kinetic coefficient κ, the anisotropy mode number j, and the current density i_L. The fractal dimension D_f, skeleton-based indicators and the inverse isoperimetric quotient consistently revealed how parameter variations affect branching, compactness, and growth rate. In particular, the inverse isoperimetric quotient IIQ proved to be an effective scalar metric for identifying the transition from compact to

dendritic growth regimes. A qualitative comparison in with experimental observations revealed that the same three characteristic morphologies identified in the simulations – compact, highly ramified, and sparse dendrites – also appear in real electrodeposited samples. This agreement supports the model capability to capture the essential features of dendritic growth in metal plating.

Future work will focus on implementing higher-order and adaptive time-integration methods, extending the model to three-dimensional geometries, extending the model to allow for plating/stripping sequences, of interest for battery dynamics, and validating the numerical predictions against experimental observations of zinc dendrite formation in real electrochemical systems, with particular attention to battery applications.

CRediT authorship contribution statement

Maria Chiara D'Autilia: Writing – original draft, Validation, Software, Methodology, Investigation, Formal analysis, Conceptualization. **Ivonne Sgura:** Writing – review & editing, Writing – original draft, Validation, Supervision, Methodology, Investigation, Funding acquisition, Conceptualization. **Massimo Frittelli:** Writing – original draft, Visualization, Validation, Methodology, Investigation, Formal analysis, Conceptualization. **Benedetto Bozzini:** Writing – review & editing, Writing – original draft, Validation, Supervision, Methodology, Investigation, Formal analysis, Data curation, Conceptualization.

Acknowledgments

I.S., M.F. and M.C.D. acknowledge financial support under the National Recovery and Resilience Plan (PNRR), Mission 4, Component 2, Investment 1.1, by the Italian Ministry of University and Research (MIUR) and by the European Union – NextGeneration EU – PRIN2022 PNRR Project Title "BAT-MEN" (BATtery Modeling, Experiments & Numerics), Project code P20228C2PP_001, CUP F53D23010020001, Grant Assignment Decree No. 1379 01/09/2023. For B.B. co-funding was received from the MESCEL project (no. 23088) under the EIT RawMaterials, part of the Horizon Europe funding.

Declaration of competing interest

The authors declare that they have no known competing financial interests or personal relationships that could have appeared to influence the work reported in this paper.

Appendix A. Numerical method

In this Appendix we detail the fully discrete Eqs. (27) for the two state variables Φ and U. Let L be the length of the spatial domain in both directions, and let N denote the number of equally spaced grid points used to discretize each direction. We define the spatial discretization step as $h = \frac{L}{N-1}$. In all the formulas that follow, the symbol $\circ$ denotes the Hadamard product, i.e., the element-wise multiplication between matrices of the same dimensions.

A.1. Spatial discretization of phase field equation (first eqn. in (22))

According to (26), the evolution of the spatially discrete phase-field variable $\Phi(t) \in \mathbb{R}^{(N-2)\times(N-2)}$ is governed by the following equation:

$$\tau \frac{d\Phi(t)}{dt} = \mathcal{F}_{\Phi}(\Phi(t), U(t)), \tag{A.1}$$

for $t \in [0, t_f]$. The operator $\mathcal{F}_{\Phi}$ in (A.1) is defined as follows:

$$\mathcal{F}_{\Phi}(\Phi(t), U(t)) = d_{\phi}\, \mathcal{E}(\Phi(t))^2 \circ \mathcal{L}(\Phi(t)) + \mathcal{D}(\Phi(t)) + \mathcal{K}_{\Phi}(\Phi(t), U(t)), \tag{A.2}$$

for $t \in [0, t_f]$. The various terms in (A.2) are detailed here below.

Surface energy anisotropy

The term $\mathcal{E}(\Phi(t))$ in (A.2) discretizes the surface energy anisotropy $\varepsilon(\theta)$ in (22) and is defined by:

$$\mathcal{E}(\Phi(t)) = \varepsilon_0 \left[1 + \delta \cos(j(\Theta(\Phi(t)) - \theta_0))\right] = \varepsilon_0 \left[1 + \delta \cos\left(j\left(\operatorname{atan}\left(\frac{\Phi(t)G}{G\Phi(t)}\right) - \theta_0\right)\right)\right], \tag{A.3}$$

which is a function of the gradient of Φ as illustrated below:

$$\Theta(\Phi(t)) = \operatorname{atan}\left(\frac{\Phi_y(t)}{\Phi_x(t)}\right) = \operatorname{atan}\left(\frac{\Phi(t)G}{G\Phi(t)}\right), \tag{A.4}$$

where Φ_x and Φ_y denote the discrete partial derivatives of Φ in the x- and y-directions, respectively, and $G \in \mathbb{R}^{(N-2)\times(N-2)}$ denotes the matrix used to discretize the gradient operator by central finite differences:

$$G = \frac{1}{2h}\begin{bmatrix} 0 & 1 & 0 & \cdots & \cdots & 0 \\ -1 & 0 & 1 & & & \vdots \\ 0 & -1 & \ddots & \ddots & & \vdots \\ \vdots & & \ddots & \ddots & 1 & 0 \\ \vdots & & & -1 & 0 & 1 \\ 0 & \cdots & \cdots & 0 & -1 & 0 \end{bmatrix}. \tag{A.5}$$

Left multiplication by G approximates the derivative in the x direction, whereas right multiplication by G approximates the derivative in the y direction.

Discrete Laplacian operator

The term $\mathcal{L}(\Phi(t))$ in (A.2) discretizes the $\Delta\phi$, where Δ is the Laplacian operator, and is defined by

$$\mathcal{L}(\Phi(t)) = T\Phi(t) + \Phi(t)T, \tag{A.6}$$

where $T \in \mathbb{R}^{(N-2)\times(N-2)}$ is the matrix representing the approximation of the second derivative in 1D:

$$T = \frac{1}{h^2}\begin{bmatrix} -2 & 1 & 0 & \cdots & \cdots & 0 \\ 1 & -2 & 1 & & & \vdots \\ 0 & 1 & \ddots & \ddots & & \vdots \\ \vdots & & \ddots & \ddots & 1 & 0 \\ \vdots & & & 1 & -2 & 1 \\ 0 & \cdots & \cdots & 0 & 1 & -2 \end{bmatrix}. \tag{A.7}$$

Left and right multiplication of $\Phi(t)$ by T approximate the second derivative in the x and y directions, respectively.

Discrete anisotropic diffusion

The anisotropic diffusion operator $\nabla \cdot \left(\varepsilon^2(\theta)\nabla\phi\right)$ in (25) can be expanded as

$$\nabla \cdot \left(\varepsilon^2(\theta)\nabla\phi\right) = \varepsilon^2(\theta)\Delta\phi + \nabla\varepsilon^2(\theta) \cdot \nabla\phi. \tag{A.8}$$

Following Biner (2017), we neglect the second term in (A.8). It follows that

$$\nabla \cdot \left(\varepsilon^2(\theta)\nabla\phi\right) \approx \varepsilon^2(\theta)\Delta\phi. \tag{A.9}$$

Therefore, thanks to (A.3), (A.6) and (A.9), the term $d_\phi\mathcal{E}(\Phi(t))\circ\mathcal{L}_\Phi(\Phi(t))$ in (A.2) is the spatial discretization of the anisotropic diffusion operator $\nabla \cdot \left(\varepsilon^2(\theta)\nabla\phi\right)$.

Mixed derivative term

The term $D(\Phi(t))$ in (A.2) spatially approximates the mixed derivative term $-\frac{\partial}{\partial x}\left(\varepsilon\varepsilon'\frac{\partial\phi}{\partial y}\right) + \frac{\partial}{\partial y}\left(\varepsilon\varepsilon'\frac{\partial\phi}{\partial x}\right)$ in (22) and is defined by

$$D(\Phi(t)) := [\Omega(\Phi(t))\circ(G\Phi(t))]\,G - G\,[\Omega(\Phi(t))\circ(\Phi(t)G)], \tag{A.10}$$

where

$$\Omega(\Phi(t)) := \mathcal{E}(\Phi(t))\circ\mathcal{E}'(\Phi(t)), \tag{A.11}$$

and $\mathcal{E}'(\Phi(t))$ is the derivative of $\mathcal{E}(\Phi(t))$ w.r.t. Θ:

$$\mathcal{E}(\Phi(t))' = -j\varepsilon_0\delta\sin\left(j\left(\Theta - \theta_0\right)\right). \tag{A.12}$$

Nonlinear kinetic term

The term $\mathcal{K}_\Phi(\Phi(t), U(t))$ in (A.2) spatially approximates the term $\phi(1-\phi)\left(\phi - \frac{1}{2} + m(u)\right)$ in (22) and is defined by

$$\mathcal{K}_\Phi(\Phi(t), U(t)) := \Phi(t)\circ(1-\Phi(t))\circ\left(\Phi(t) - \frac{1}{2} + m(U(t))\right), \tag{A.13}$$

with

$$m(U(t)) = \frac{\alpha}{\pi}\operatorname{atan}\left(\gamma\left(U(t) - u_{\text{nucl}}\right)\right). \tag{A.14}$$

A.2. Spatial discretization of mass transport (second eqn. in (22))

According to (26), the evolution of the spatially discrete concentration variable $U(t) \in \mathbb{R}^{(N-2)\times(N-2)}$ is governed by the following equation:

$$\frac{dU(t)}{dt} = \mathcal{F}_U(\Phi(t), U(t)), \tag{A.15}$$

where

$$\mathcal{F}_U(\Phi(t), U(t)) = d_u\, \mathcal{L}(U(t)) + \mathcal{K}_U(\Phi(t), U(t)). \tag{A.16}$$

In (A.16), the operator $\mathcal{L}$ is the discrete Laplacian defined in (A.6), while the kinetic term $\mathcal{K}_U$ is defined as follows:

$$\mathcal{K}_U(\Phi(t), U(t)) = \kappa \mathcal{V}_\Phi(t) \circ \frac{\|\nabla\Phi(t)\|}{(1/i_L)\,\mathcal{V}_\Phi(t) + \|\nabla\Phi(t)\|}, \tag{A.17}$$

where

$$\mathcal{V}_\Phi(t) := \frac{d\Phi(t)}{dt}, \qquad \|\nabla\Phi(t)\| := \sqrt{(\Phi_x(t))^{\circ 2} + (\Phi_y(t))^{\circ 2}} := \sqrt{(G\Phi(t))^{\circ 2} + (\Phi(t)G)^{\circ 2}}, \tag{A.18}$$

where the notation $^{\circ 2}$ indicates the componentwise square.

Summary of the spatially discretized system

Hence, after the spatial discretization, the resulting ODE system (not yet accounting for boundary conditions) in matrix form is given by:

$$\begin{cases} \tau \frac{d\Phi}{dt} = d_\phi\, \mathcal{E}^2(\Phi) \circ (T\Phi + \Phi T) + (\Omega(\Phi) \circ (G\Phi))\, G - G\,(\Omega(\Phi) \circ (\Phi G)) + \mathcal{K}_\Phi(\Phi, U); \\ \frac{dU}{dt} = d_u\,(TU + UT) + \mathcal{K}_U(\Phi, U), \end{cases} \tag{A.19}$$

for $t \in [0, t_f]$.

Implementation of boundary conditions

Depending on the boundary conditions applied along each direction, suitable corrections need to be added to the spatially discrete system (A.19). Specifically, recalling the boundary conditions (23):

- for the x-direction, Dirichlet boundary conditions are applied, therefore the matrices T and G do not need any correction, following Settanni and Sgura (2016), Sgura et al. (2012). We thus utilize $T_2 = T$ and $G_2 = G$ along the x-direction;
- for the x-direction, the *non-homogeneous* nature of the Dirichlet boundary conditions requires the usage (illustrated below) of the following boundary correction terms:

$$\Phi_{\mathrm{BC}_T} := \frac{\Phi_{\mathrm{BC}}}{h^2}; \quad \Phi_{\mathrm{BC}_G} := \frac{\Phi_{\mathrm{BC}}}{2h}; \quad U_{\mathrm{BC}_T} := \frac{U_{\mathrm{BC}}}{h^2}, \tag{A.20}$$

  where Φ_{BC} and U_{BC} are the $\mathbb{R}^{(N-2)\times N}$ matrices defined by

$$(\Phi_{\mathrm{BC}})_{ij} := \begin{cases} \phi_0(x_j, y_i) & \text{if } j = 1, N \text{ (i.e. } x_j = 0, L); \\ 0 & \text{otherwise,} \end{cases} \tag{A.21}$$

$$(U_{\mathrm{BC}})_{ij} := \begin{cases} u_0(x_j, y_i) & \text{if } j = 1, N \text{ (i.e. } x_j = 0, L); \\ 0 & \text{otherwise,} \end{cases} \tag{A.22}$$

  where the functions ϕ_0 and u_0 are defined in (24).
- for the y-direction, Neumann boundary conditions are applied. Therefore, for the y-direction, we employ the corrected matrices T and G defined as follows, following Settanni and Sgura (2016), Sgura et al. (2012):

$$G_1 := G + \frac{B}{h}, \quad T_1 := T + \frac{B}{h^2}, \quad \text{where } B := \frac{1}{3}\begin{bmatrix} 4 & -1 & 0 & \cdots & 0 & 0 & 0 \\ 0 & 0 & 0 & \cdots & 0 & 0 & 0 \\ \vdots & \vdots & \vdots & & \vdots & \vdots & \vdots \\ 0 & 0 & 0 & \cdots & 0 & 0 & 0 \\ 0 & 0 & 0 & \cdots & 0 & -1 & 4 \end{bmatrix};$$

Thus, the spatial discretization with boundary corrections is:

$$\begin{cases} \tau \frac{d\Phi}{dt} = d_\phi\, \mathcal{E}^2 \circ \left(T_1\Phi + \Phi T_2 + \Phi_{\mathrm{bc}_T}\right) + \left(\Omega \circ (G_1\Phi)\right) G_2 - G_1 \left(\Omega \circ \left(\Phi G_2 + \Phi_{\mathrm{bc}_G}\right)\right) + \mathcal{K}_\Phi(\Phi, U); \\ \frac{dU}{dt} = d_u \left(T_1 U + U T_2 + U_{\mathrm{bc}_T}\right) + \mathcal{K}_U(\Phi, U), \end{cases} \tag{A.23}$$

for $t \in [0, t_f]$.

Appendix B. Morphological indicators for dendritic structures

In this Appendix, we provide a detailed description of the quantitative morphological indicators employed to characterize the dendritic structures obtained from the numerical simulations. These indicators are: the *skeleton-based metrics*, the *fractal dimension* (D_f) and the *inverse isoperimetric quotient* (IIQ). The purpose of these metrics is to quantify various properties of the simulated dendritic structures.

B.1. Skeleton-based morphological metrics

We extract detailed topological information from dendritic structures using skeletonization (Lee et al., 1994). This process reduces each dendrite to a one-pixel-thick *medial axis* while preserving its connectivity and branching structure, and provides a convenient representation from which several morphometric indicators can be derived.

From the skeleton, we compute standard descriptors such as

- **Total Skeleton Length** L_S. The *total skeleton length* is defined as the number of pixels forming the skeleton and provides a measure of the dendrite's overall extent.
- **Branching points** n_B A *branching point* is a pixel of the skeleton with more than two neighboring pixels, indicating a bifurcation.
- **End Points** n_E An *end point* is a terminal pixel of the skeleton, i.e. a pixel with only one neighbor, corresponding to a dendritic tip.
- **Branch density**. The *branch density* is defined as

$$d_B = \frac{\text{Number of Branching Points}}{\text{Total Skeleton Length}},$$

  and quantifies how frequently the dendrite branches along its length.
- **Mean tortuosity**. The *mean tortuosity* measures the winding of dendritic branches, intended as their deviation from a straight line. For each branch, tortuosity is defined as

$$m_T = \frac{L}{D},$$

  where L is the actual path length along the branch and D is the straight-line Euclidean distance between the branch endpoints. The mean tortuosity is obtained by averaging T over all branches of the dendrite.

Implementation notes

Skeletonization is performed using MATLAB's `bwmorph` function with the `'skel'` operation. Branching points and end points are identified by counting the number of neighboring pixels for each skeleton pixel. Together, these metrics provide a detailed quantitative description of dendritic morphology, complementing the fractal analysis.

B.2. Fractal dimension via box-counting algorithm

The *fractal dimension* is a measure of the geometric complexity of a structure that exhibits self-similarity over multiple scales. In the context of dendritic growth, it provides a measure of the interface's morphological complexity, capturing how intricately the dendrite fills the spatial domain.

Box-counting algorithm

The fractal dimension D_f is estimated using the *box-counting method*, a robust technique widely used for binary images and spatial patterns (Genau et al., 2013; Ohsasa et al., 2015; Warriner et al., 2020). The algorithm is implemented as follows:

1. Cover the computational domain containing the dendritic interface with a uniform grid of square boxes of side length $\varepsilon > 0$.
2. For decreasing values of ε, count the number of boxes $N(\varepsilon)$ that contain at least a portion of the dendritic interface. The interface can be defined by thresholding the phase-field variable ϕ, for example as the set of points where $\phi = 0$ or within a narrow band around zero.
3. Repeat the counting for a range of box sizes ε, spanning multiple scales as allowed by the spatial resolution.
4. Assume a scaling relation of the form

$$N(\varepsilon) \sim C\varepsilon^{-D_f}.$$

   Taking logarithms gives a linear relation:

$$\log N(\varepsilon) \approx -D_f \log \varepsilon + C;$$

5. The fractal dimension D_f is obtained as the slope of the linear fit of the data $(-\log \varepsilon, \log N(\varepsilon))$.

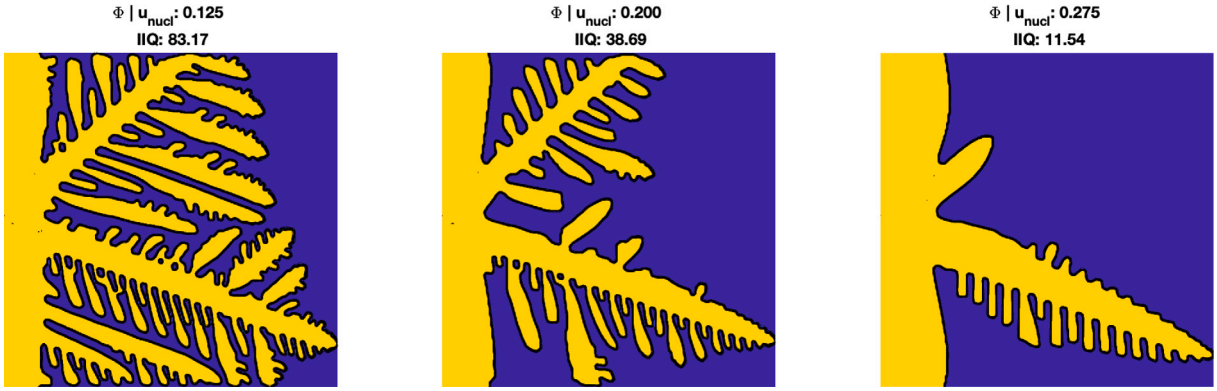

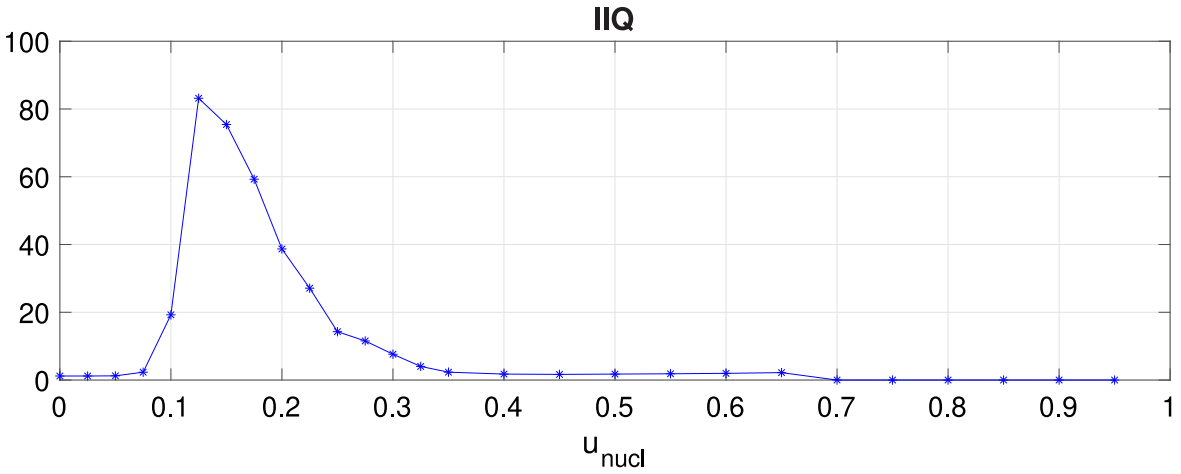

Fig. C.9. Impact of u_{nucl} on the IIQ. The IIQ has a steep increasing trend for lower values of u_{nucl} and then decreases asymptotically to 0.

Interpretation

A fractal dimension D_f between 1 and 2 indicates that the structure is more complex than a simple curve (dimension 1) but does not completely fill the plane (dimension 2). Higher values of D_f correspond to more branched, intricate, and space-filling dendritic structures. Monitoring D_f across different parameter values allows to establish the impact of parameters on space-filling properties of the resulting dendrites.

B.3. Isoperimetric quotient and inverse as a dendritic growth metric

The *isoperimetric quotient* (IQ) is a classical metric used to quantify the compactness of a two-dimensional set $S \subset \mathbb{R}^2$ (Osserman, 1978):

$$\text{IQ} := \frac{4\pi A}{P^2}, \tag{B.1}$$

where A is the area of S and P is its perimeter. The IQ reaches its maximum value of 1 when S is a perfect circle, which is the most compact shape in 2D. For branched or elongated structures, IQ is strictly less than 1. Since we are primarily interested in *irregular, dendritic structures*, we define the *inverse isoperimetric quotient* (IIQ) as:

$$IIQ = \frac{P^2}{4\pi A}, \tag{B.2}$$

which serves as a *dendritic growth index*:

- IIQ = 1 corresponds to a perfect circle (minimal dendritic character).
- IIQ > 1 indicates increasingly branched or irregular morphologies.

Properties and computation

The IIQ is dimensionless and scale-invariant, making it suitable for comparisons across different simulations. It reflects the relative increase in boundary length per unit area, a hallmark of dendritic structures. An application is shown in Section 5.2. Computation is straightforward from binary images using image processing tools such as MATLAB's `bwboundaries` (for perimeter extraction) and `nnz` or `regionprops` (for area computation).

Appendix C. Impact of u_{nucl} on the IIQ

In this Appendix we explore the dependence of the IIQ on the dimensionless equilibrium concentration u_{nucl}. To this end, we fix the model parameters as in Table 1 with $\kappa = 1.6$ and $i_L = 40$ and we solve the model for several values of $u_{\text{nucl}} \in (0, 1)$. In Fig. C.9 we show the numerical solutions (ϕ component) obtained for $u_{\text{nucl}} = 0.125, 0.2, 0.275$ and we plot the IIQ of the final dendrite against u_{nucl}. The maximum value of IIQ is attained around $u_{\text{nucl}} = 0.125$, Therefore, we chose $u_{\text{nucl}} = 0.2$ throughout the paper, as it leads to significant dendrite formation.

Data availability

Data will be made available on request.

References

Arguello, M., Gumulya, M., Derksen, J., Utikar, R., & Calo, V. (2022a). Phase-field modeling of planar interface electrodeposition in lithium-metal batteries. *Journal of Energy Storage*, *50*, Article 104627. http://dx.doi.org/10.1016/j.est.2022.104627.

Arguello, M. E., Labanda, N. A., Calo, V. M., Gumulya, M., Utikar, R., & Derksen, J. (2022b). Dendrite formation in rechargeable lithium-metal batteries: Phase-field modeling using open-source finite element library. *Journal of Energy Storage*, *53*, Article 104892. http://dx.doi.org/10.1016/j.est.2022.104892.

Arguello, M., Labanda, N., Calo, V., Gumulya, M., Utikar, R., & Derksen, J. (2023). Three-dimensional experimental-scale phase-field modeling of dendrite formation in rechargeable lithium-metal batteries. *Journal of Energy Storage*, *62*, Article 106854.

Biner, S. B. (2017). Programming phase-field modeling. Springer International Publishing, http://dx.doi.org/10.1007/978-3-319-41196-5.

Bozzini, B., D'Urzo, L., & Mele, C. (2007). A novel polymeric leveller for the electrodeposition of copper from acidic sulphate bath: a spectroelectrochemical investigation. *Electrochimica Acta*, *52*(14), 4767–4777. http://dx.doi.org/10.1016/j.electacta.2007.01.015.

Bozzini, B., D'Urzo, L., Re, M., & De Riccardis, F. (2008). Electrodeposition of Cu from acidic sulphate solutions containing cetyltrimethylammonium bromide (CTAB). *Journal of Applied Electrochemistry*, *38*(11), 1561–1569. http://dx.doi.org/10.1007/s10800-008-9598-z.

Bozzini, B., Mele, C., & D'Urzo, L. (2006a). Electrodeposition of Cu from acidic sulphate solutions in the presence of PEG-Part II visible electroreflectance spectroscopy measurements during electrodeposition. *Journal of Applied Electrochemistry*, *36*(1), 87–96. http://dx.doi.org/10.1007/s10800-005-9026-6.

Bozzini, B., Mele, C., D'Urzo, L., Giovannelli, G., & Natali, S. (2006b). Electrodeposition of Cu from acidic sulphate solutions in the presence of PEG: an electrochemical and spectroelectrochemical investigation–Part I. *Journal of Applied Electrochemistry*, *36*(7), 789–800. http://dx.doi.org/10.1007/s10800-006-9139-6.

Caramia, V., & Bozzini, B. (2015). Potential-dependent reactivity of adsorbed cyanide during the electrodeposition of silver from cyanocomplexes: a study based on in-situ surface-enhanced Raman spectroscopy. *Transactions of the IMF*, *93*(2), 82–88. http://dx.doi.org/10.1179/00202967l4Z.000000000207.

Chen, L., Zhang, H. W., Liang, L. Y., Liu, Z., Qi, Y., Lu, P., Chen, J., & Chen, L.-Q. (2015). Modulation of dendritic patterns during electrodeposition: A nonlinear phase-field model. *Journal of Power Sources*, *300*, 376–385. http://dx.doi.org/10.1016/j.jpowsour.2015.09.055.

D'Autilia, M. C., Sgura, I., & Simoncini, V. (2020). Matrix-oriented discretization methods for reaction–diffusion PDEs: Comparisons and applications. *Computers & Mathematics with Applications*, *79*(7), 2067–2085. http://dx.doi.org/10.1016/j.camwa.2019.10.020.

Genau, A. L., Freedman, A. C., & Ratke, L. (2013). Effect of solidification conditions on fractal dimension of dendrites. *Journal of Crystal Growth*, *363*, 49–54. http://dx.doi.org/10.1016/j.jcrysgro.2012.09.044.

He, C., Gou, Q., Hou, Y., Wang, J., You, X., Yang, N., Tian, L., Xie, G., & Chen, Y. (2024). Growth and inhibition of zinc anode dendrites in Zn-air batteries: Model and experiment. *Chinese Journal of Chemical Engineering*, *67*, 268–281. http://dx.doi.org/10.1016/j.cjche.2023.11.016.

Hong, Z., & Viswanathan, V. (2018). Phase-field simulations of lithium dendrite growth with open-source software. *ACS Energy Letters*, *3*(7), 1737–1743. http://dx.doi.org/10.1021/acsenergylett.8b01009.

Jian, Q., Sun, J., Li, H., Guo, Z., & Zhao, T. (2024). Phase-field modeling of zinc dendrites growth in aqueous zinc batteries. *International Journal of Heat and Mass Transfer*, *223*, Article 125252. http://dx.doi.org/10.1016/j.ijheatmasstransfer.2024.125252.

Kobayashi, R. (1993). Modeling and numerical simulations of dendritic crystal growth. *Physica D: Nonlinear Phenomena*, *63*(3–4), 410–423. http://dx.doi.org/10.1016/0167-2789(93)90120-p.

Lee, T.-C., Kashyap, R. L., & Chu, C.-N. (1994). Building skeleton models via 3-D medial surface axis thinning algorithms. *CVGIP: Graphical Models and Image Processing*, *56*(6), 462–478. http://dx.doi.org/10.1006/cgip.1994.1042.

Li, C. e. a. (2025). A dynamically bare metal interface enables reversible magnesium electrodeposition at 50 mah cm-2. *Joule*, *9*(2), http://dx.doi.org/10.1016/j.joule.2024.11.007.

Liang, L., Q, Y., Xue, F., Bhattacharya, S., Harris, S. J., & Chen, L.-Q. (2012). Nonlinear phase-field model for electrode-electrolyte interface evolution. *Physical Review E*, *86*(5), http://dx.doi.org/10.1103/physreve.86.051609.

Liu, Z., Li, Y., Ji, Y., Zhang, Q., Xiao, X., Yao, Y., Chen, L.-Q., & Qi, Y. (2021). Dendrite-free lithium based on lessons learned from lithium and magnesium electrodeposition morphology simulations. *Cell Reports Physical Science*, *2*(1), Article 100294. http://dx.doi.org/10.1016/j.xcrp.2020.100294.

Ohsasa, K., Natsume, Y., Sekiya, T., & Hatayama, T. (2015). Evaluation of dendrite morphology using fractal dimension and dimensionless perimeter in unidirectionally solidified Al-Si Alloys. *IOP Conference Series: Materials Science and Engineering*, *84*, Article 012033. http://dx.doi.org/10.1088/1757-899x/84/1/012033.

Osserman, R. (1978). The isoperimetric inequality. *Bulletin of the American Mathematical Society*, *84*(6), 1182–1238. http://dx.doi.org/10.1090/s0002-9904-1978-14553-4.

Popov, K. I., Djokić, S. S., & Grgur, B. N. (2002). Fundamental aspects of electrometallurgy. Springer, http://dx.doi.org/10.1007/0-306-47564-2_3.

Qi, G., Liu, X., Dou, R., Wen, Z., Zhou, W., & Liu, L. (2024). A three-dimensional multiphysics field coupled phase field model for lithium dendrite growth. *Journal of Energy Storage*, *101*, Article 113899. http://dx.doi.org/10.1016/j.est.2024.113899.

Qi, G., Liu, X., Yi, X., Dou, R., Wen, Z., Zhou, W., & Liu, L. (2025). Electrochemical-mechanical coupled phase-field modeling for lithium dendrite growth in all-solid-state lithium metal batteries. *Journal of Energy Chemistry*, *110*, 80–87. http://dx.doi.org/10.1016/j.jechem.2025.06.015.

Qiao, D., Liu, X., Dou, R. o., Wen, Z., Zhou, W., & Liu, L. (2022). Quantitative analysis of the inhibition effect of rising temperature and pulse charging on Lithium dendrite growth. *Journal of Energy Storage*, *49*, Article 104137. http://dx.doi.org/10.1016/j.est.2022.104137.

Settanni, G., & Sgura, I. (2016). Devising efficient numerical methods for oscillating patterns in reaction–diffusion systems. *Journal of Computational and Applied Mathematics*, *292*, 674–693. http://dx.doi.org/10.1016/j.cam.2015.04.044.

Sgura, I., Bozzini, B., & Lacitignola, D. (2012). Numerical approximation of Turing patterns in electrodeposition by ADI methods. *Journal of Computational and Applied Mathematics*, *236*(16), 4132–4147. http://dx.doi.org/10.1016/j.cam.2012.03.013.

Warriner, W. E., Friess, J., & Genau, A. (2020). Fractal Correlation Dimensions Analysis of Al–Si Dendrites. *Metallography, Microstructure, and Analysis*, *9*(4), 561–569. http://dx.doi.org/10.1007/s13632-020-00672-z.

Yao, S., Kan, X., Zhou, R., Ding, X., Xiao, M., & Cheng, J. (2021). Simulation of dendritic growth of a zinc anode in a zinc–nickel single flow battery using the phase field-lattice Boltzmann method. *New Journal of Chemistry*, [ISSN: 1369-9261] *45*(4), 1838–1852. http://dx.doi.org/10.1039/d0nj05528j.

Yi, X., Qi, G., Liu, X., Depcik, C., & Liu, L. (2024). Challenges and strategies toward anode materials with different lithium storage mechanisms for rechargeable lithium batteries. *Journal of Energy Storage*, *95*, Article 112480. http://dx.doi.org/10.1016/j.est.2024.112480.

Yuan, X., He, C., Wang, J., You, X., Chen, Y., Gou, Q., Yang, N., Xie, G., & Hou, Y. (2024). Inhibition of zinc dendrite growth in zinc-air batteries by alloying the anode with Ce and Yb. *Journal of Alloys and Compounds*, *970*, Article 172523. http://dx.doi.org/10.1016/j.jallcom.2023.172523.